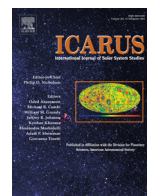




ELSEVIER

Contents lists available at ScienceDirect

Icarus

journal homepage: [www.elsevier.com/locate/icarus](http://www.elsevier.com/locate/icarus)

## Modeling glacial flow on and onto Pluto's Sputnik Planitia<sup>☆</sup>

O.M. Umurhan<sup>a,b,\*</sup>, A.D. Howard<sup>c</sup>, J.M. Moore<sup>a,b</sup>, A.M. Earle<sup>d</sup>, O.L. White<sup>a</sup>, P.M. Schenk<sup>e</sup>, R.P. Binzel<sup>d</sup>, S.A. Stern<sup>f</sup>, R.A. Beyer<sup>a,b</sup>, F. Nimmo<sup>g</sup>, W.B. McKinnon<sup>h</sup>, K. Ennico<sup>a</sup>, C.B. Olkin<sup>f</sup>, H.A. Weaver<sup>i</sup>, L.A. Young<sup>f</sup>

<sup>a</sup> National Aeronautics and Space Administration (NASA), Ames Research Center, Space Science Division, Moffett Field, CA 94035, United States

<sup>b</sup> SETI Institute, 189 Bernardo Ave, Suite 100, Mountain View, CA 94043, United States

<sup>c</sup> University of Virginia, Department of Environmental Sciences, P.O. Box 400123 Charlottesville, VA 22904-4123, United States

<sup>d</sup> Massachusetts Institute of Technology, Department of Earth, Atmospheric and Planetary Sciences, Cambridge, Massachusetts 02139, United States

<sup>e</sup> Lunar and Planetary Institute, 3600 Bay Area Blvd. Houston, TX 77058, United States

<sup>f</sup> Southwest Research Institute, Boulder, CO 80302, United States

<sup>g</sup> Earth and Planetary Science, University of California, Santa Cruz, CA 95064, United States

<sup>h</sup> Department of Earth and Planetary Sciences, Washington University, St. Louis, MO 63130, United States

<sup>i</sup> Johns Hopkins University Applied Physics Laboratory, Laurel, MD, 20723, United States

### ARTICLE INFO

#### Article history:

Received 13 May 2016

Revised 8 December 2016

Accepted 18 January 2017

Available online xxx

#### MSC:

00-01

99-00

#### Keywords:

Pluto

Ices

Ices, mechanical properties

Geological processes

Pluto, surface

### ABSTRACT

Observations of Pluto's surface made by the New Horizons spacecraft indicate present-day N<sub>2</sub> ice glaciation in and around the basin informally known as Sputnik Planitia. Motivated by these observations, we have developed an evolutionary glacial flow model of solid N<sub>2</sub> ice that takes into account its published thermophysical and rheological properties. This model assumes that glacial ice flows laminarily and has a low aspect ratio which permits a vertically integrated mathematical formulation. We assess the conditions for the validity of laminar N<sub>2</sub> ice motion by revisiting the problem of the onset of solid-state buoyant convection of N<sub>2</sub> ice for a variety of bottom thermal boundary conditions. Subject to uncertainties in N<sub>2</sub> ice rheology, N<sub>2</sub> ice layers are estimated to flow laminarily for thicknesses less than 400–1000 m. The resulting mass-flux formulation for when the N<sub>2</sub> ice flows as a laminar dry glacier is characterized by an Arrhenius–Glen functional form. The flow model developed is used here to qualitatively answer some questions motivated by features we interpret to be a result of glacial flow found on Sputnik Planitia. We find that the wavy transverse dark features found along the northern shoreline of Sputnik Planitia may be a transitory imprint of shallow topography just beneath the ice surface suggesting the possibility that a major shoreward flow event happened relatively recently, within the last few hundred years. Model results also support the interpretation that the prominent darkened features resembling flow lobes observed along the eastern shoreline of the Sputnik Planitia basin may be the result of a basally wet N<sub>2</sub> glacier flowing into the basin from the pitted highlands of eastern Tombaugh Regio.

© 2017 Elsevier Inc. All rights reserved.

### 1. Introduction

The New Horizons flyby of Pluto has revealed a planetary surface exhibiting evidence of recent geological activity (Stern et al., 2015; Moore et al., 2016). In a compendium study found in this volume (Howard et al., 2017, this volume) we have examined the evidence for both ancient and recent glacial flow on Pluto based

on imaging data taken by the MVIC and LORRI cameras as well as spectroscopic data obtained by the LEISA instrument.<sup>1</sup> The aim of this work is to develop a physical model framework to use with investigating various scenarios pertaining to N<sub>2</sub> ice glacial flow into and within Sputnik Planitia (SP, hereafter and note that all place names on Pluto are informal).<sup>2</sup> N<sub>2</sub>, CH<sub>4</sub> and CO are observed to be

<sup>☆</sup> All place names of the Pluto system are informal.

\* Corresponding author at: National Aeronautics and Space Administration (NASA), Ames Research Center, Space Science Division, Moffett Field, CA 94035, United States.

E-mail addresses: [orkan.umurhan@gmail.com](mailto:orkan.umurhan@gmail.com), [orkan.m.umurhan@nasa.gov](mailto:orkan.m.umurhan@nasa.gov) (O.M. Umurhan).

<sup>1</sup> These are cameras and instruments onboard New Horizons: MVIC (Multispectral Visible Imaging Camera) is the medium-resolution color wide-angle “push-broom” camera while LORRI (LONg Range Reconnaissance Imager) is the high-resolution framing panchromatic camera. LEISA (Linear Etalon Imaging Spectral Array) is the 256 channel imaging spectrometer (Stern et al., 2015; Reuter et al., 2008).

<sup>2</sup> An earlier version of this manuscript referred to this region as “Sputnik Planum”. The designation of this feature from *planum* to *planitia* is a result of recent

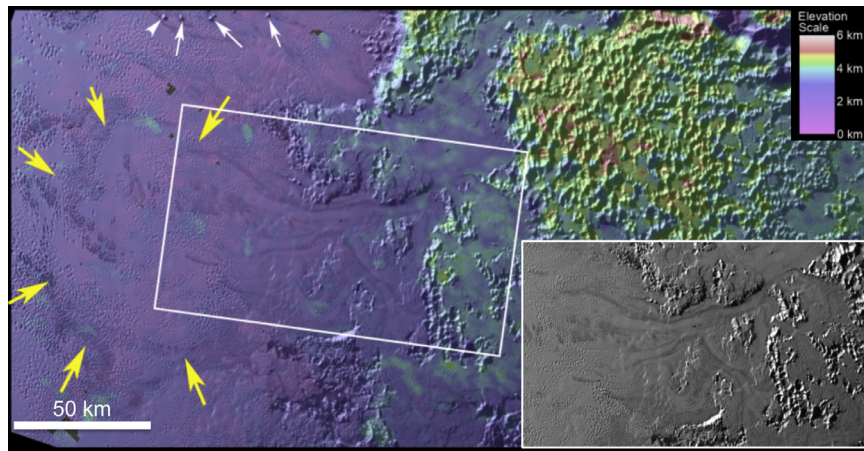


**Fig. 1.** A LORRI image section of eastern Sputnik Planitia abutting the pitted highlands of ETR color-coded for elevation. Streak patterns emanating from the higher elevations are seen to follow an apparent flow path to the lower reaches of Sputnik Planitia. Yellow arrows indicate the extent of flow lobes. Examples indicating englaciated debris shown with white arrows. In this image, north is up. Location of this section is found in Fig. 3.

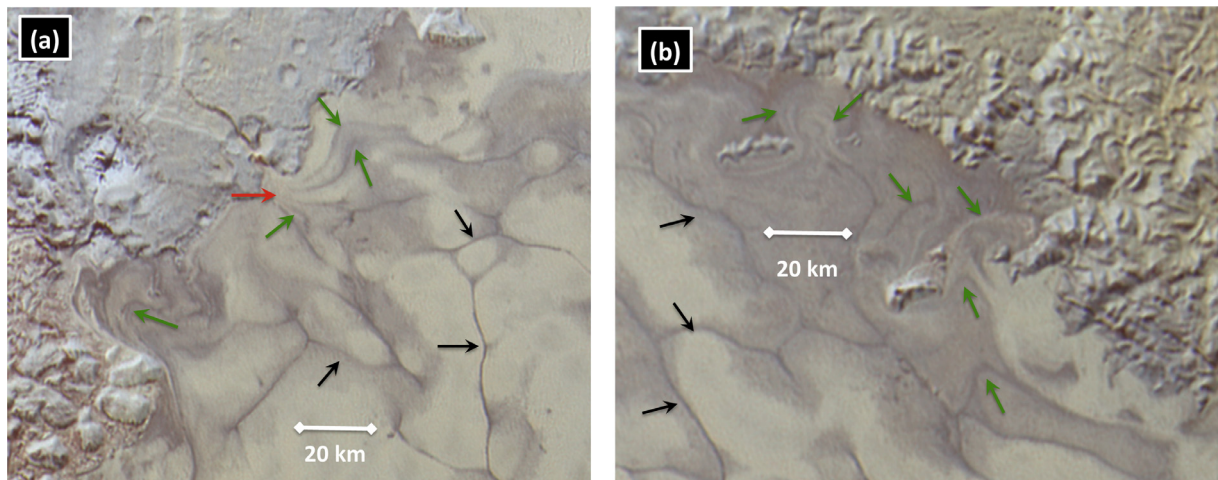


**Fig. 2.** MVIC sections of the northwestern (left panel) and northeastern (right panel) shorelines of Sputnik Planitia. The dark ovoid patterning found on the lower portion of both images (black arrows) have been interpreted as downwellings involving solid-state convection of  $N_2$  ice (McKinnon et al., 2016). The near shoreline dark patterning (green arrows) may be indicative of either flow advection of recently inactivated convective downwellings or an imprint of surface topography beneath the observable surface. The red arrow indicates a possible undersurface drainage point (Howard et al. 2017, this volume). In both images, north is up. Location of this section is found in Fig. 3. (For interpretation of the references to color in this figure legend, the reader is referred to the web version of this article.)

present within and around SP (Grundy et al., 2016) as well as in Pluto's atmosphere (Gladstone et al., 2016). Based on the relative overabundance of  $N_2$  compared to CO on SP, we shall assume that it is the primary material undergoing glacial flow – however, this should be subject to further scrutiny.

Fig. 1 depicts a prominent example of features suggesting recent  $N_2$  glacial flow from the pitted uplands of eastern Tombaugh Regio (ETR, hereafter) and down onto the plains of SP. Dark streaks reminiscent of medial moraines, emanating from the highlands, connect to the floor of SP by commonly passing through narrow throats 2–5 km wide. The dark streaks terminate on SP with a pattern resembling flow lobes. There are also lone protruding  $H_2O$  ice blocks with trailing dark streaks leading towards the higher elevation  $N_2$  icy flats, highly suggestive that these structures may be englaciated debris (Howard et al., 2017, this volume).

Interestingly, flow also appears to be moving from the interior of SP out toward both its northern and southern shores (Howard et al. 2017, this volume). Fig. 2(a-b) depicts examples of indi-

cators of flow toward Sputnik Planitia's northern shoreline. The lower portion of Fig. 2(a) depicts ovoid patterning interpreted to be downwellings associated with solid-state convection of  $N_2$  ice (Stern et al., 2015; Moore et al., 2016; McKinnon et al., 2016). However the near shoreline manifestation of the dark patterns takes on a markedly different quality, becoming increasingly wavy closer to shore. Fig. 2(b) depicts similar features with the additional appearance of transverse surface patterning suggestive of viscous flow around an obstacle. Two ways in which these observations may be interpreted are: (i) the northward moving  $N_2$  ice flow advects darkened, possibly inactive, convective downwelling zones giving rise to the observed near shoreline gentle undulations or (ii) the wavy patterns are an imprint of topography beneath SP's surface.

In order to test the viability of scenarios pertinent to Pluto's apparent present-day glacial flow, a physical model needs to be constructed that takes into account, among other things, the known thermophysical and rheological properties of solid  $N_2$  and CO under the very cold physical conditions of Pluto's surface. Of the latter molecule, very little laboratory data is available under Plutonian surface conditions, but given CO's similar molecular bonding structure to  $N_2$ , we assume that its behavior resembles that of

topographic refinements indicating that this planar region has an elevation below the mean radius of Pluto.

$N_2$  under these conditions (Moore et al., 2016). Most importantly, however, is the fact that the rheology of solid  $N_2$  has not been very well constrained to date (see discussion in Section 2.2) and since many of the results we report in this study depend upon the rheology, any future developments and updates regarding solid  $N_2$ 's rheology will likely necessitate revising many of the results quoted here. Despite these current uncertainties, we can use this model to answer some broad qualitative questions about the nature of the observed surface flow.

According to experiments and analyses done to date (see Section 2.2 for further details),  $N_2$  ice behaves as a viscous fluid with a viscosity somewhere between  $H_2O$  ice in slightly subfreezing terrestrial conditions ( $\eta \sim 10^{12} \text{ Pa} \cdot \text{s}$  at stresses of  $10^5 \text{ Pa}$  (Durham et al., 2010)), and room temperature pitch or bitumen ( $\eta \sim 10^8 \text{ Pa} \cdot \text{s}$ ). Conditions affecting the flow of  $N_2$  ice include the depth of the flowing  $N_2$  layers, the incoming geothermal flux and the temperature conditions both at the bases and surfaces of such layers. The layer depth and surface temperatures determine whether or not the  $N_2$  ice moves as a “basally wet”, “wet”, or “dry” glacier, and whether or not a glacier of a given thickness experiences buoyant solid state convection.<sup>3</sup> A preliminary physical model should include other various landform modification processes like accretion/decrecence, i.e., continuous growth/retreat by accretion/decretion, Howard et al. (2012), and bedrock scouring. Of course, to what degree these various landform modifying effects are operating on today's Pluto is unclear, but we formally include it in our construction with the expectation that these inputs will become clear once more research is done.

With today's surface temperature on Pluto being  $\sim 38.5 \text{ K}$ , Grundy et al. (2016), getting solid  $N_2$  to surpass its triple point at the base of the layer requires layer thickness of up to 0.1–1 km or more (Moore et al., 2016; McKinnon et al., 2016).  $N_2$  collected on sloping channels will likely advect into depressions (including SP) long before one can build up that much material owing to the apparent low viscosity of solid  $N_2$ . However, occasional basal melt of  $N_2$  ice layers in the pitted highlands surrounding SP may have occurred in Pluto's recent geologic past. Two recent studies, Earle and Binzel (2015) and Earle et al. (2017, this volume), have shown that Pluto's obliquity variations (Dobrovolskis and Harris, 1983) coupled with the precession of Pluto's orbital apsis can give rise to conditions in which Pluto's surface temperatures might get as high as  $\sim 55\text{--}60 \text{ K}$  for stretches of time lasting 2–3 decades. Under those conditions,  $N_2$  ice layers as little as 200–400 m thick may undergo basal melt which could give rise to episodic, possibly flood-like, drainage events. Similarly, however, basal melt can also result in steady-state drainage of liquid  $N_2$  into the  $H_2O$  ice bedrock below – especially if the substrate is highly porous and/or supports a deeply extended crack system.

At this early stage of discovery, these observations and reflections point to many questions about the history and conditions of  $N_2$  ices on Pluto. In this study we start with two modest scenarios which we examine using a vertically integrated physical model whose development is detailed in Section 4. The two questions we seek to address with our mathematical model are

1. Are the transverse wavy dark features near the northern edges of SP an imprint of bottom topography?
2. Are the flow lobe features and deposits indicated by similarly darkened features in Fig. 1 evidence of basal melting and consequent basal sliding style flow?

The short answer to each question is: (a) Our model results show that bottom topography can be embossed on the surface of

flowing  $N_2$  ice. However, due to the viscous nature of the ice, the imprint fades in a few decades suggesting that such features are transitory and short. (b) A scenario in which  $N_2$  ice flows as a basally wet glacier, i.e., a glacier whose base is in a liquid state, better reproduces the quality of the observed flow lobe features, however, it does not rule out that the observed features are a result of purely dry glacial flow.

This work is organized in the following way. In Section 2, we review known relevant information on solid  $N_2$  and CO, and we provide a table summarizing their thermophysical properties. Section 2.2 provides a summary of the current knowledge of  $N_2$  rheology including estimates of its stress-strainrate relationships as well as the corresponding viscosities. Section 2.3 discusses the near surface thermal profiles likely to be present within  $N_2$  ice. Section 2.4 considers the range of possible surface temperatures on Pluto over the course of its obliquity variations over the last 3 million years. Section 3 examines the conditions for the onset of thermal convection in  $N_2$  ice heated from below by a static  $H_2O$  ice bedrock conducting Pluto's geothermal heat-flux. The answer to this question is important because it determines the validity of the glacial model developed in the section that follows.

Section 4 contains a description of the flow model and mass-flux law we construct for  $N_2$  glacial flow appropriate for the surface of Pluto followed by an examination of various e-folding relaxation timescales for  $N_2$  ice structures of various sizes, depths and extents using the formulated mass-flux law. Owing to its highly technical nature, we have relegated to Appendix C the detailed mathematical development of the vertically integrated flow model we adopt which includes the primary assumption that the flow is laminar, neither experiencing buoyant convection nor shear flow induced turbulence. Section 5 begins with detailing the model landscapes we use for our simulations and is concluded by model results concerning the two hypothetical questions posed above. Section 6 reviews our efforts and rounds out with some thoughts on future directions.

## 2. General physical properties

### 2.1. Thermophysical properties of $N_2$ and CO

$N_2$  and CO have similar molecular bond physics (primarily Van der Waals) and their collective properties as a solid ought to be similar to one another. However, while some laboratory data is available for  $N_2$  at the temperatures and pressures of relevance for Pluto, comparatively scant laboratory data is available for CO. Nonetheless, we have compiled and summarized this data in tabular form in Table 1. We note an important quality of  $N_2$ , namely that it is relatively insulating compared to  $H_2O$  ice: in fact the conductivity of nitrogen ice is  $K(N_2) \approx (1/20)K(H_2O)$ , where the figure for  $H_2O$  ice conductivity  $K(H_2O)$  in the temperature range 36–63 K is taken from reference (Schmitt et al., 1998). It is also noteworthy that the coefficient of thermal expansion of nitrogen ice is also nearly 5 times that of  $H_2O$  ice at these temperatures.

Both  $N_2$  and CO have two solid phases:  $\alpha$  and  $\beta$ . The crystal structure of the  $\alpha$  phase is cubic while the  $\beta$  phase is a hexagonal close-packed crystal (Scott, 1976; Fracassi et al., 1986). The  $\alpha - \beta$  phase transition in CO occurs at  $T = T_{\alpha\beta}(\text{CO}) = 61.55 \text{ K}$  while the corresponding transition occurs for  $N_2$  at  $T = T_{\alpha\beta}(N_2) = 35.6 \text{ K}$  (Fray and Schmitt, 2009) with transition enthalpies of 22.4 kJ/kg and 8.2 kJ/kg for CO and  $N_2$  respectively (Fracassi et al., 1986; Giauque and Clayton, 1933). We note that the surface pressures are sufficiently low as to not effect the quality of the emerging crystal structure (Scott, 1976). It is also worth noting that for the surmised surface temperatures of Pluto, CO is in its  $\alpha$ -phase while  $N_2$  is in its  $\beta$  phase. While CO and  $N_2$  are fully soluble in the range of temperatures of interest to us, the rheological

<sup>3</sup> A basally wet glacier here is understood to be a glacier whose base is liquid. This should be distinguished from a wet glacier which is, throughout its entirety, a mixture of ice and liquid between ice grains.

**Table 1**  
Known properties of solid N<sub>2</sub> and CO near their triple points.

Molecule	$T_m/P_m^a$ (K/bars)	$\rho_s$ (g/cm <sup>3</sup> )	$C_p$ (kJ/kg · K)	$K$ (W/mK)	$\alpha^b$ ( $\times 10^{-3}/K$ )	$\Delta E_s^c$ (kJ/kg)	$\Delta E_f^d$ (kJ/kg)
N <sub>2</sub>	63.10/0.11 <sup>e</sup>	0.99–0.95 <sup>f</sup>	1.35–1.65 <sup>f</sup>	0.215–0.200 <sup>f</sup>	1.7–2.7 <sup>f</sup>	224.9 <sup>g</sup>	25.7 <sup>g</sup>
CO	68.13/0.14 <sup>h</sup>	1.01–0.97 <sup>i</sup>	1.29–2.32 <sup>j,k</sup>	0.350–0.280 <sup>l</sup>	n/a	296.4 <sup>k</sup>	29.6 <sup>m</sup>

<sup>a</sup> Melt temperature and pressures at triple point.

<sup>b</sup> Coefficient of thermal expansion.

<sup>c</sup> Heat of sublimation in vicinity of  $T_m$ .

<sup>d</sup> Heat of fusion in vicinity of  $T_m$ .

<sup>e</sup> Ref. Fray and Schmitt (2009).

<sup>f</sup> Range quoted for  $\beta$ -phase of N<sub>2</sub> between 36–63 K, ref. Scott (1976).

<sup>g</sup> Ref. Giaque and Clayton (1933).

<sup>h</sup> See Fray and Schmitt (2009); Goodwin (1985)

<sup>i</sup> Range quoted for  $\alpha$ -phase of CO between 41 and 61.5 K, based on compiled data shown in Fig. 1 of ref. Fracassi et al. (1986).

<sup>j</sup> Note that in  $\alpha$ -phase these quantities deviate from linear profile.

<sup>k</sup> Experimentally determined, ref. Fracassi et al. (1986); Kelley (1935)

<sup>l</sup> Range quoted for  $\alpha$ -phase of CO between 45–65 K, based on experimental data shown in Fig. 4 of Ref. Konstantinov et al. (2006).

<sup>m</sup> Ref. Clayton and Giaque (1932).

properties of a composite mixture of the two molecular species is currently unknown, requiring detailed laboratory work in the near future. The uncertainty in the rheological properties are likely compounded when a third constituent, like CH<sub>4</sub>, is added to the mix.

## 2.2. Rheological properties of N<sub>2</sub> and CO

As of the writing of this work, there are two known studies pertaining to the rheological properties of N<sub>2</sub> in solid-state for the temperatures of interest to us, i.e. between 30 K and 63 K. There is no known analogous laboratory analysis of CO.<sup>4</sup> As such, and primarily owing to the similar molecular bond structures of both N<sub>2</sub> and CO (see last section), we cautiously consider the qualitative and quantitative properties of CO ices to be similar to N<sub>2</sub>. We briefly review the aforementioned N<sub>2</sub> studies here:

*Non-Newtonian creep of laboratory annealed solid N<sub>2</sub>.* Yamashita et al. (2010) consider the rheological properties of laboratory annealed N<sub>2</sub> under a variety of tangential stresses and at two temperatures (45 K and 56 K). They show that its stress,  $\sigma$ , and strain-rate,  $\dot{\epsilon}$ , behave with a power-law relationship given by

$$\dot{\epsilon} = A(T)\sigma^n(T), \quad (1)$$

where the prefactor  $A$  and the index  $n$  (in the vicinity of 2.1) are both temperature dependent. The prefactor  $A(T)$  was fit to an Arrhenius form in Moore et al. (2016) and shown to have an effective activation energy  $E_a$  of about 3.5 kJ/mole or, equivalently

$$A(T) = A_{45} \exp\left(\frac{T_a}{45 K} - \frac{T_a}{T}\right),$$

$$A_{45} = 0.005s^{-1}(\text{MPa})^{-n(T)}, \quad (2)$$

where the activation temperature is  $T_a = E_a/k = 422$  K. The temperature dependence of the index was determined assuming a linear fit to be given by the expression  $n(T) = 2.1 + 0.0155(T/K - 45)$ . With this in mind, we assume a *visco-plastic viscosity* which is defined as

$$\eta \equiv \frac{\partial \sigma}{\partial \dot{\epsilon}}, \quad (3)$$

(Hughes, 2009). Together with this we input the power-law form for the laboratory annealed N<sub>2</sub> ice experiment to find

$$\eta = \frac{1}{nA\sigma^{n-1}}. \quad (4)$$

Under conditions where the tangential stresses are about 10 kPa (0.1 bar) the viscosity of N<sub>2</sub> ice at 45 K is about  $1.6 \times 10^{10}$  Pa · s.

<sup>4</sup> Probably owing to its hazardous biological toxicity.

*Newtonian creep of N<sub>2</sub> ice grains.* In Kirk (1990); Eluszkiewicz and Stevenson (1990); Eluszkiewicz (1991) the rheological properties of N<sub>2</sub> ice grains were examined in the framework of both Coble creep and Nabarro–Herring (NH) creep, both considered diffusional processes ( $n = 1$ ) and often considered collectively as grain-boundary sliding (GBS) (Durham et al., 2010). As opposed to the non-Newtonian case just discussed, we assume the viscosity of grains is linear (and, hence, “Newtonian”). The grain rheologies discussed in these aforementioned studies are based on a nuclear magnetic resonance (NMR) study of N<sub>2</sub> grains done by Esteve and Sullivan (1981). Coble creep is based on the diffusion of molecules along grain boundaries while NH creep is based on the diffusion of molecules through grains themselves. The general trend is that NH-creep dominates Coble creep when a material approaches its melt temperatures. Based on the scant data available for N<sub>2</sub>, NH creep will dominate Coble creep for temperatures greater than about 25 K for grain diameters in the vicinity of 1 mm (see Appendix A).

Thus, for N<sub>2</sub> ice grain spheres of radial size  $d_g$  the effective volume diffusion rate through grains  $D_{0v}$  was empirically assessed by Esteve and Sullivan (1981) (studying the self-diffusion of N<sub>2</sub> ice laced with Ar impurities) to be given by

$$D_{0v} = 1.6 \times 10^{-7} e^{-T_v/T} \text{ m}^2/\text{s}, \quad (5)$$

where the experimentally determined activation temperature  $T_v \approx 1030$  K relates to the corresponding experimentally determined activation energy,  $E_v \approx 8.6$  kJ/mole, via  $E_v \equiv kT_v$ , where  $k$  is the Boltzmann constant ( $= 1.38 \times 10^{-23}$  m<sup>2</sup>kg s<sup>-2</sup>K<sup>-1</sup>). From this relationship an effective *linear viscosity* can be written as (Eluszkiewicz and Stevenson, 1990; Eluszkiewicz, 1991)

$$\eta = \frac{kTd_g^2}{42D_{0v}\Omega}, \quad (6)$$

where  $\Omega$  is the volume of a single N<sub>2</sub> molecule ( $= 4.9 \times 10^{-29}$  m<sup>3</sup>). This expression can be rewritten in a way more revealing and relevant to the surface of Pluto

$$\eta_{nh} = 1.84 \times 10^{16} \left(\frac{d_g}{\text{mm}}\right)^2 \left(\frac{T}{45 K}\right) \exp\left(\frac{T_v}{T} - \frac{T_v}{45 K}\right), \quad (7)$$

in units of Pa · s. We have designated this effective viscosity  $\eta_{nh}$  in order to make it clear that this is the purely “Newtonian”, diffusional creep instance of this form.

While the non-Newtonian properties of N<sub>2</sub> ice grains are not fully explored beyond that described above, we posit, by analogy to extensive studies done on the creep properties of H<sub>2</sub>O ice, that diffusion GBS creep of N<sub>2</sub> ice grains may be enhanced by dislocation accommodated GBS. Assuming that the stresses in subsurface Plutonian ices sit well within the range of 1–10<sup>5</sup> Pa and the grain

sizes are within 0.001–1 mm, and accepting the posited analogy between  $N_2$  and  $H_2O$  ices, an examination of the various expected rheological properties of  $H_2O$  ices showcased in Fig. 6 of Durham et al. (2010) suggests that  $N_2$  ice grains might have a “superplastic” weakly non-Newtonian flavor with a stress-strain power-law index of  $n = 1.8$ . Provided this is the case for  $N_2$  ice grains, then according to the definition of viscosity in Eq. (3) we suggest that their collective viscous behavior might be described by

$$\eta = \eta_{nh} \left( \frac{\dot{\epsilon}_2^{(nh)}}{\dot{\epsilon}_2} \right)^{(1-n)/n} = \eta_{nh} \left( \frac{\dot{\epsilon}_2^{(nh)}}{\dot{\epsilon}_2} \right)^{-4/9}, \quad (8)$$

where  $\dot{\epsilon}_2^{(nh)}$  is a reference value of the second invariant of the strain tensor, a figure currently unknown and requiring future laboratory work to determine.

### 2.3. On the thermal profiles of Plutonian $N_2/CO$ ice layers

The thermal gradients and timescales of  $N_2/CO$  ice-layers are important to assess. Assuming ice-layers too shallow for convection to occur, we can estimate the vertical temperature gradient across a layer of depth  $H$ . A recent study by Robuchon and Nimmo (2011), investigating the interior thermal history of Pluto, suggests that the current-day geothermal heat-flux amounts to a few  $10^{-3}$  W/m<sup>2</sup>. We adopt as a reference value for this interior flux of  $F_{pi}^{(ref)} = 4 \times 10^{-3}$  W/m<sup>2</sup>. From the numbers compiled in Section 2.1 for  $N_2$ ,<sup>5</sup> we adopt a value for the conductivity  $K \approx 0.2$  W/mK and assigning  $F_{pi}$  to be the emergent heat flux, we find that the mean interior temperature gradient  $\bar{T}_z \equiv F_{pi}/K$ , or

$$\bar{T}_z \approx 20 \left( F_{pi}/F_{pi}^{(ref)} \right) \text{ } ^\circ\text{K/km}. \quad (9)$$

We note that due to its insulating nature compared to  $H_2O$  ice, the vertical temperature gradient in such ices is very high. The thermal diffusion coefficient through solid  $N_2$  can be estimated from the definition  $\kappa \equiv K/\rho_s C_p \approx 0.66 \times 10^{-6}$  m<sup>2</sup>/s where we adopt a value for the heat capacity  $C_p = 1.65$  kJ/kg K. Thus, one can estimate the e-folding thermal relaxation time across a layer of width  $H$  by  $\tau \equiv H^2/(4\pi^2\kappa)$ , which we express as (Moore et al., 2016),

$$\tau = 6 \times 10^{-3} (H/m)^2 \oplus \text{yr} = (H/H_0)^2 \oplus \text{yr}, \quad (10)$$

in which  $\oplus \text{yr}$  is one terrestrial year. The reference scale  $H_0 \approx 12.9$  m, which says that a layer of approximately 13 m will equilibrate into its conductive profile in one Earth year. Thus, unless deposition rates greatly exceed this figure, the temperature profile of the glacier should be roughly equal to the conductive equilibrium profile. Calculations performed and quoted by Young (2012) and Grundy et al. (2016) estimate sublimation/deposition rates on present-day Pluto to be in the range 1–10 cm/Pluto-yr which suggests that it is reasonable to assume a glacier whose interior temperature is in conductive equilibrium.

### 2.4. Surface temperatures over time

We undertake a momentary detour in our discussion and consider the past history of Pluto’s surface temperatures. The import of this consideration is to give a justification for the potential of  $N_2$  ice glaciers to undergo basal melt for certain stretches of time (see Section 4). The idea we have in mind here is the following: with the emerging geothermal flux held fixed, a rise in the surface temperature will steadily induce a concomitant rise in the temperature of the base. Thus, even if the surface does not approach melting point, the base of the glacier will more easily achieve this

<sup>5</sup> Keeping in mind that all quoted quantities have a temperature dependence but we consider them sufficiently weak for our current considerations.

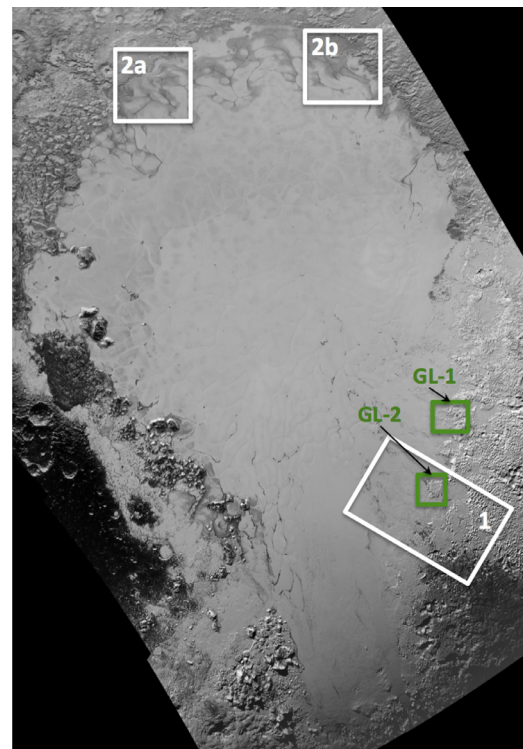


**Fig. 3.** A larger view of Sputnik Planitia with the locations of Figs. 1–2 indicated (white boxes). The green boxes indicate sample landscapes (“GL-1”, “GL-2”) are used as test bedrock landforms for modeling done in Section 5. (For interpretation of the references to color in this figure legend, the reader is referred to the web version of this article.)

state owing to its relative warmth. With a wet base, the flow and evolution properties of  $N_2$  glaciers will exhibit significantly different qualities from those glaciers that remain basally frozen.

While the surface temperature of today’s Pluto is just under 40 K, the surface was likely to be much warmer in its past. Pluto’s obliquity variations (Dobrovolskis and Harris, 1983) coupled with the precession of its orbital apsides implies that the total amount of seasonally averaged radiant energy received on a given hemispheric surface will significantly vary over timescales of approximately three million  $\oplus$  years. This has direct influence on the resulting surface pressures and temperatures (Earle and Binzel, 2015) and can give rise to surface temperatures approaching 55–60 K lasting for about 20–30 Pluto years under conditions of favorable alignment of Pluto’s orbital apsis and obliquity extremes.

Fig. 4a–b shows the surface temperature results of two Pluto climate models whose details may be found in Earle et al. (2017, This Volume). The model, based on the one constructed by Trafton (1984), and its parameter inputs are summarized here: Pluto’s heliocentric distance and sub-solar latitudes are calculated as a function of time based on the calculation of Dobrovolskis et al. (1997). A simplified albedo and volatile map is used which assumes polar caps with latitudinal extent of either  $\pm 45^\circ$  (Fig. 4) or  $\pm 60^\circ$  (Fig. 4b). The polar caps are modeled as having a variety of different albedos (0.1, 0.3, or 0.6). To represent the thermal influence of Tombaugh Regio, Earle et al. (2017, this volume) include a bright (albedo = 0.6) volatile patch extending from  $-30^\circ$  to  $+45^\circ$  with a longitudinal extent of  $45^\circ$ . For different trials, two extremes of a range of plausible emissivity values are examined (e.g. 0.6 or 0.9). These inputs are then incorporated into the energy balance equation model, originally presented in Trafton (1984), and used to determine the global temperature as a function of time. Note that the solutions developed do not take into account the possibility of time lags associated with thermal inertia effects.

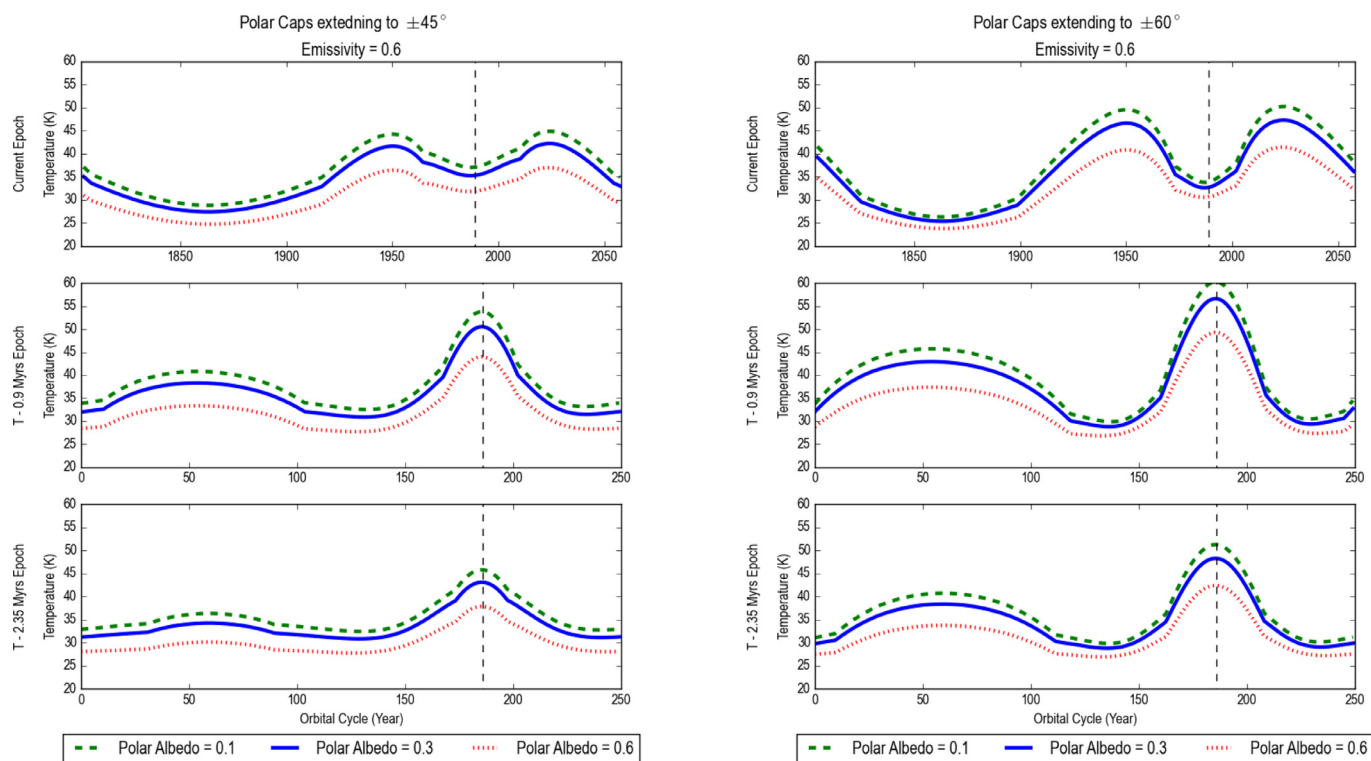


**Fig. 4.** Surface temperatures of Pluto over a 3 Myr obliquity/precessional cycle. Model assumes the presence of a landmass representing Tombaugh Regio (see text). The ice emissivity is assumed to be 0.6. Solutions are shown for three different values of the polar albedos. Left panel shows a suite of solutions assuming that the polar caps extend down to  $\pm 45^\circ$  latitude while right panel shows solutions with the polar caps extended further to  $\pm 60^\circ$  latitude.

The results are fairly typical: During extreme insolation conditions when Pluto's orbital apsides and obliquity are favorably aligned, maximum surface temperatures persist for 20–30 Pluto years. When the polar caps extend to  $\pm 60^\circ$  latitude, the surface temperatures become very close to the melt temperature of  $N_2$ . This means that one may have circumstances in which *relatively shallow* layers of  $N_2$  ice may experience basal melting for stretches of time and this, in turn, can have important physical consequences in the flow response of  $N_2$  ice layers, i.e., whether or not the layer exhibits basally wet or dry flow – see further discussion of this in Section C.1.

For example, during these climate extremes, the surface temperatures get as high as 55 K which, assuming a conductive temperature gradient within the ice of 20 K/km, would correspond to a layer thickness just under 400 m before melt occurs at the base of the glacier (the minimum pressure requirement for melt, of about  $10^4$  Pa (Fray and Schmitt, 2009), is satisfied at that depth).

### 3. Onset of convection

The eastern shoreline of SP, and various locations along the other boundaries of SP, indicate there are regions in which convection is either absent or occurring very weakly (McKinnon et al., 2016). While the subsurface basin profile of SP is unknown, estimates as to the depth of various sections of SP can be made based on the distinctive lack of obvious signs of buoyant solid-state convection. One of the important inputs for this study is to estimate an upper limit of the thickness of an  $N_2/CO$  ice layer before it starts to undergo solid-state convection. In addition to knowing when one ought to expect convection to occur in, SP the glacial flow modeling detailed in Section 4 also implicitly assumes that the flowing glacial ice is more or less laminar, which we assume to be the case if the layer thicknesses are less than that for onset of convection. It is therefore important to get a good sense of the

conditions under which convection is expected to occur. Thermal convection in terrestrial ice glaciers has been examined as a possible explanation for the origin of ice streams which can drain up to 90% of glacial ice (Hughes, 2009).

It is not useful to perform here an exhaustive examination of the transition into convection given all the possible formulations of  $N_2$ 's rheology outlined in Section 2.2. We are interested, however, in getting a good order of magnitude figure for this onset. Thus for our calculation here we assume a static Newtonian layer of  $N_2$  ice grains and consider the onset to convection assuming the viscosity is given by  $\eta = \eta_{nh}$ , as defined in Eq. (7). This analysis then becomes amenable to a linear stability calculation. We assume the layer is in conductive thermal equilibrium with its interior which is a reasonable assumption given the thermal equilibration times we estimated in the previous section. The vertical horizontally uniform temperature profile is  $T(z) = T_s - \bar{T}_{0z}(z - z_s)$  where  $\bar{T}_{0z}$  is given in Eq. (9),  $z_s$  is the location of the surface, and  $T_s$  is the temperature of the surface for which we set as the present day surface temperature on  $N_2$  ice of 38.5 K.

Due to the temperature contrast, the viscosity at the top and bottom of a layer will be different and, therefore, we consider the Rayleigh number  $Ra$  as measured at the base of a given layer. We hereafter consider the viscous diffusion  $\nu \equiv \eta/\rho_s$  and define  $p \equiv \ln(\nu_t/\nu_b)$  to be the natural logarithm of the ratio of the viscosities between the top and bottom layers,  $\nu_t$  and  $\nu_b$  respectively. The Rayleigh number  $Ra$  at the base is therefore defined as

$$Ra \equiv \frac{g\alpha\rho_s H^4 \bar{T}_{0z}}{\kappa\nu_b}, \quad (11)$$

where  $g = 0.642 \text{ m/s}^2$  is the surface gravity of Pluto and  $\alpha$  is the coefficient of thermal expansion whose values of  $N_2$  ice are given in Table 1. The onset to convection is a function of the two parameters  $p$  and  $Ra$ . We note that  $Ra$  has an Arrhenius law dependence due to the temperature dependence on  $\nu_b$ , as well as a  $d_g^{-2}$  de-

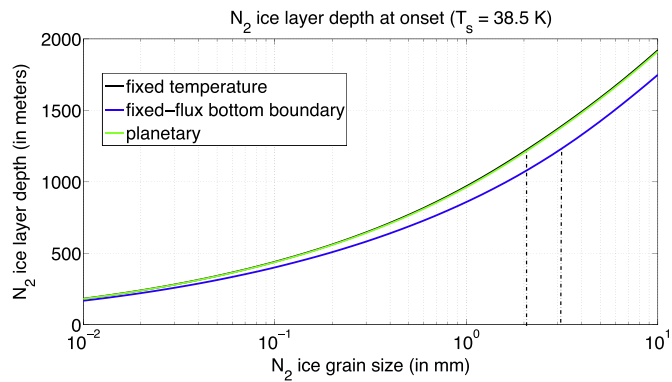


**Fig. 5.** Minimum layer thickness for the onset of convection as a function of  $N_2$  ice-grain size. Figure shows solution of transition to convection assuming the top of the convecting layer has fixed upper temperature of  $T = 38.5$  K and vertical temperature gradient  $\bar{T}_{oz} = 20$  K/km. Solutions for three different bottom thermal boundary conditions shown: fixed-temperature, fixed-flux and “planetary” – detailed in Appendix B. Solutions determined use the Frank-Kamenskii approximation (Solomatov, 2012). Vertical hatched lines denote critical grain-sizes for which the temperature at the layer’s base corresponds to  $T_m = 63.1$  K, i.e., the triple-point melt temperature for  $N_2$ .

pendence on ice-grain size. The detailed form of Ra, as well as the assumptions and solution methods employed to assess this transition to convection, is detailed in Appendix B.

We are interested here in three questions: (1) For a given  $N_2$  ice-grain size  $d_g$ , how deep a layer of  $N_2$  ice on Pluto does one need to initiate solid-state convection? (2) At onset of solid-state convection, what is the critical viscosity contrast as a function of  $d_g$ ? (3) What is the temperature of the base of the layer at onset to convection as a function of  $d_g$ ? The answer to these questions are graphically displayed in Figs. 5–6 and we use these figures for our future referencing henceforth. We note that the depth of the ice-layer must be thicker for larger ice-grains and this is to be expected since solid-state ices composed of larger ice-grains are characterized by larger viscosities.

We also note there are critical values of the ice-grain size for which the transition into convection occurs at depths for which the base temperature,  $T_b \equiv T_s + H\bar{T}_{oz}$ , corresponds to the melt temperature  $T_m$  at the triple-point for  $N_2$ . The bottom panel of Fig. 6 shows the results of a model in which the surface temperature  $T_s = 38.5$  K and where  $\bar{T}_{oz} = 20$  K/km, and we see that  $T_m$  corresponds to about 63 K for ice-grains of size  $d_g = 2 - 3$  mm (depending upon which boundary condition is employed). Cross-referencing this critical grain-size with the corresponding critical value of the

depth of the layer upon which transition is predicted to occur (Fig. 5) shows that this happens at layer thicknesses  $H \approx 1.2$  km.

We conclude by noting that the onset of convection in sheared flows is known to occur at (and often significantly) higher values of Ra as compared to their non-sheared equivalents, e.g., see the discussion and references in Landuyt and Lerley (2012); Goluskin et al. (2014). As such, we consider the Ra numbers for transition to be lower bounds for the onset of convection in down-gradient flowing  $N_2/CO$  ice. In practice this means for us that flowing ice layers probably move laminarily down-gradient for layer thicknesses greater than the limits suggested by conditions indicated in Fig. 5. When revisions to  $N_2$  rheologies become available, many of the figures quoted in this work will need to be revised.

#### 4. Landform evolution modeling

Partly motivated by our findings regarding the onset of convection described in Section 3, we treat the glacially flowing ice as a single laminarily flowing viscous fluid in the infinite Prandtl number limit. This assumption permits the use of vertically integrated modeling methods (e.g., see discussions in Hindmarsh, 2004; Benn and Evans, 2010) whose asymptotic validity is rooted in perturbation analyses (e.g., Balmforth et al., 2003). The assumption of laminar flow is valid so long as the moving glacial ice layers are not thick enough to experience buoyant convection. Vertically integrated modeling is expected to be valid so long as the horizontal length scale of the layer dwarves the vertical extent of the layer – in the glaciology literature this is often referred to as the shallow sheet approximation (SSA) (Hindmarsh, 2004). Appendix C contains a detailed exposition of the derivation of the vertically integrated SSA model we use and interested readers are directed there.

The model setup is sketched in the cartoon found in Fig. 7. We consider a single spatiotemporally varying ice component whose local vertical thickness as a function of horizontal location is given by  $H(x, y, t)$ . The ice sits on a bedrock whose surface is located at  $z = Z_b(x, y, t)$ . Note in Appendix C we develop a model in which the bedrock may be convertible into ice due to various landform modifying processes, but for our purposes here in this study we treat the bedrock as static. The local elevation is given by  $z = Z(x, y, t) = H(x, y, t) + Z_b(x, y)$ . The evolution of the local ice layer is given by the (scaled) horizontal divergence of the corresponding mass flux

$$\partial_t H = \nabla \cdot \mathbf{q}, \quad (12)$$

where the *total mass-flux* is given as the sum of a “dry” and “basally wet” glacial flow,

$$\mathbf{q} = q_0 \nabla Z, \quad q_0 = q_{sl} + q_{dry}. \quad (13)$$

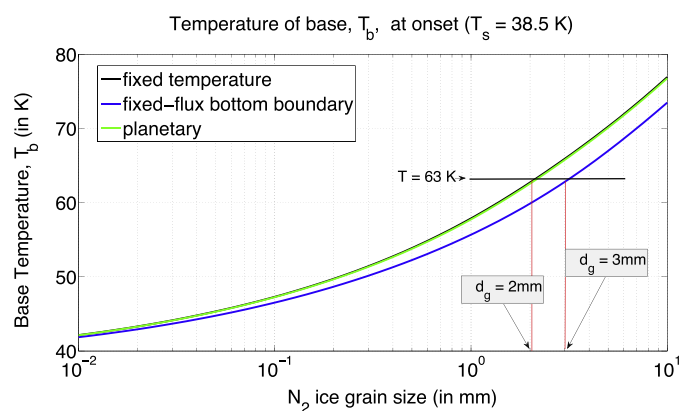
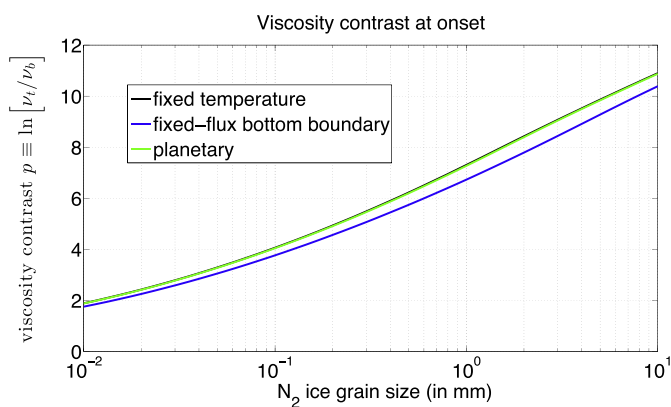


**Fig. 6.** (Left panel) Base temperature at transition into buoyant convection. (Right panel) Viscosity contrast for the onset of convection. Results shown in both panels assessed for parameters shown in Fig. 5. The grain-size values corresponding to melt temperatures at the triple-point for  $N_2$  are designated  $d_g \approx 2$  mm for fixed-temperature and planetary thermal boundary conditions at the base while  $d_g \approx 3$  mm for fixed-flux bottom boundaries.

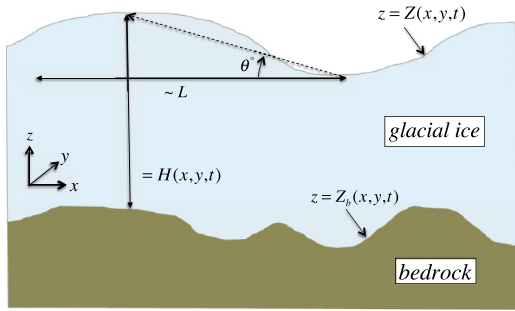


**Fig. 7.** Glacial ice modeling schematic. Evolving glacial ice of thickness  $H(x, y, t)$  with surface elevation position  $z = Z(x, y, t)$  and bedrock surface  $z = Z_b(x, y, t)$ . All quantities are space and time dependent. The angle  $\theta$  describes the grade of the surface feature with horizontal scale  $\sim L$ .

The dry component of the mass-flux coefficient is given by

$$q_{\text{dry}} = g_Q \exp\left[\frac{H/H_a}{1 + H/H_{\Delta T}}\right] q_{\text{glen}},$$

$$q_{\text{glen}} \equiv \frac{A_s (\rho_s g H)^n H^2}{n + 2} \frac{S^{n-1}}{(1 + S^2)^{n/2}}. \quad (14)$$

The model adopts a non-Newtonian Glen law formulation (Section 2.2) modified to take into account the strongly insulating nature of nitrogen ice (Section 2.1). The classical Glen law part of the expression is contained in  $q_{\text{glen}}$  where the Glen law index is  $n$ .  $S$  is the local scalar tangent of the surface, i.e.,  $S \equiv |\nabla Z|$ .  $A_s = A(T_s)$  is the value of the Arrhenius prefactor expression, found in Eq. (2), evaluated at the surface temperature  $T_s$ . The parameters appearing in the dry glacial mass flux formula, Eq. (15),  $H_a$  and  $H_{\Delta T}$ , are given by

$$H_{\Delta T} = T_s / \bar{T}_{0z}, \quad H_a = T_s^2 / (T_a \bar{T}_{0z}),$$

where  $T_a, \bar{T}_{0z}$  are respectively, the activation temperature of  $N_2$  ice (Section 2.1) and the vertical temperature gradient inside the ice (Section 2.3). The order 1 numerical parameter  $g_Q$ , which is a corrective term depending upon the rheology of the flowing material, is described in detail in Appendix C. For all of our subsequent modeling we adopt a constant value of  $g_Q = 0.5$ .

The mass flux coefficient of the basal sliding component is given by

$$q_{\text{sl}} = \frac{H}{|\nabla Z|} \begin{cases} u_{\text{sl}0}, & H > H_m, \\ \mathbf{0}, & 0 < H < H_m. \end{cases} \quad (15)$$

The physical meaning of the model is that once a minimum thickness  $H_m$  is achieved, the base of the layer experiences melt.  $H_m$  generally depends upon many physical inputs including latitude, local sloping angle of the surface and the emergent geothermal flux (i.e.,  $\bar{T}_{0z}$ ), but for our purposes in this study we adopt a constant value for it. The wet base adds a constant velocity  $u_{\text{sl}0} \hat{\mathbf{t}}$  to the flowing glacier, where  $\hat{\mathbf{t}} \equiv \nabla Z / |\nabla Z|$  is a unit vector indicating the map-projected direction of the local downslope of the ice. The speed  $u_{\text{sl}0}$  is the magnitude of the basal flow which we treat as a model input parameter, but it may generally be considered to be a function of other inputs like total overburden pressure and temperature. This physical model is derived from terrestrial glacial flow modeling.<sup>6</sup>

<sup>6</sup> Caution is advised. It is likely that a basally wet  $N_2$  ice layer may behave differently than basally wet terrestrial  $H_2O$  ice glaciers owing primarily to the lower density of liquid  $N_2$  compared to its solid phase. Sufficiently thick layers of low viscosity liquid  $N_2$  underneath an ice layer should lead to Rayleigh–Taylor instabilities which would, consequently, lead to vertical mixing of the liquid  $N_2$  with the overlying ice. Further theory is required in this instance.

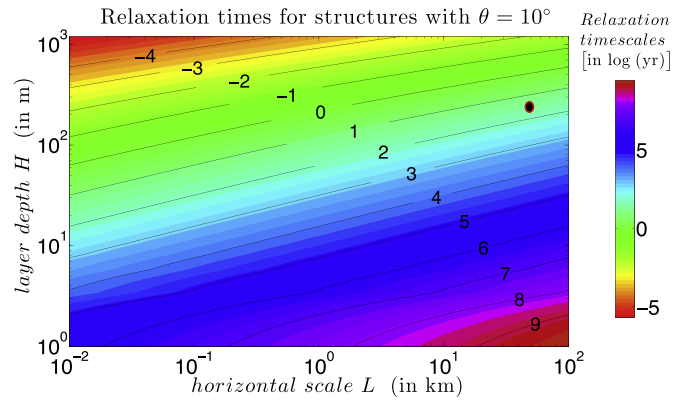


**Fig. 8.** Flow timescales  $\tau$  for glacial ice structures composed of  $N_2$  ice characterized by the rheology of Yamashita et al. (2010): glacial ice configurations with surface sloping grades of  $\theta = 10^\circ$ . Flow timescales are presented for a range of horizontal and layer-depths  $L$  and  $H$  respectively. The surface temperature of the ice is  $T_s = 38.5$  K with a vertical temperature gradient  $\bar{T}_{0z} = 20$  K/km. Other parameters are  $n = 2.1$ ,  $H_a \approx 175$  m,  $H_{\Delta T} = 1925$  m with  $g_Q = 0.5$ .

We reflect upon the functional dependence on the dry mass-flux coefficient  $q_{\text{dry}}$ , which scales as

$$\sim H^{n+2} \exp\left(\frac{H/H_a}{1 + H/H_{\Delta T}}\right),$$

indicating its significant deviation from the classical Glen Law form used for terrestrial glacial ice modeling, i.e., the classical form contained in the expression  $q_{\text{glen}}$ . We refer to this composite form as the Arrhenius–Glen mass-flux dependency. This new form reflects the Arrhenius prefactor of  $N_2$ 's rheology, which becomes significant because of the strongly insulating nature of  $N_2$  that promotes the development of strong temperature gradients inside a conducting layer of  $N_2$  ice. This occurs on a relatively short period of time (see discussion in Section 2.3).

## 5. Some model results

We present here a preliminary examination of the two questions/scenarios posed in the Introduction. We work with model landscapes adapted from digital elevation models (DEM) of two regions on the eastern side of SP (further detailed below in Section 5.2). We treat these surfaces as the primary bedrock and onto them we add a certain amount of  $N_2$  ice and observe the response. We solve Eqs. (12)–(15) using a stripped down version of MARSSIM (Howard, 2007) in which the glacial flow law is assessed using both either a second or fourth order correct finite-difference flux method. The program solves the equations of motion in a doubly periodic domain.

### 5.1. Flow timescales - some estimates

We can make certain estimates regarding the flow time-scales associated with various ice-configurations assuming dry  $N_2$  ice layers. We adopt the rheology of Yamashita et al. (2010) – but we keep in mind that all estimates made here will need to be revised when future improvements to  $N_2$  ice's rheology are made available.

An e-folding flow timescale,  $\tau$ , may be assigned to surface features of horizontal length  $L$ , vertical height  $H$ , and surface gradients characterized by the grade angle  $\theta$ . Assuming that the bedrock is static, temporal variations in  $Z$  are the same as temporal variations in  $H$ . Thus, the left hand side of the evolution Eq. (12) may be approximated by  $H/\tau$ . Using the form for the mass-flux given by Eq. (13) together with the approximate form for the dry  $N_2$  ice mass-flux  $q_{\text{dry}}$  in Eq. (14), and the assumption that horizontal variations of surface features scale with  $L$  (see Fig. 7), the order-of-

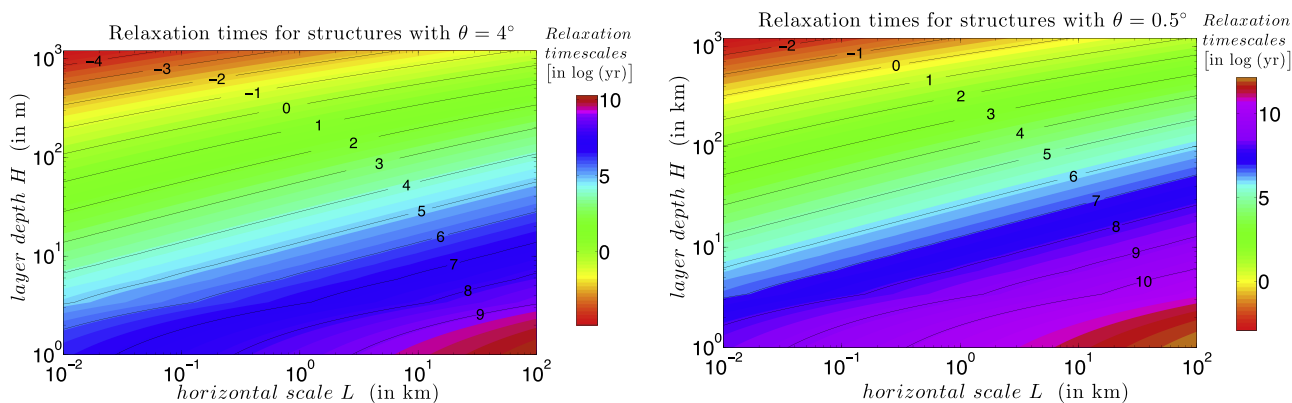


**Fig. 9.** Like Fig. 8 except for ice configurations with surface sloping grades of  $\theta = 4^\circ$  (top panel) and  $\theta = 0.5^\circ$  (bottom panel).

magnitude measure of the right-hand-side of Eq. (12) is given by  $\sim L^{-1}|q_0 \tan \theta|$ . Putting these two estimates together produces the following expression for the rate  $\tau^{-1}$ ,

$$\begin{aligned} \tau^{-1} &\approx \frac{|q_0 \tan \theta|}{HL}, \\ &= g_c \frac{H A_s (\rho_s g H)^n}{L^{n+2}} \exp \left[ \frac{H/H_a}{1 + H/H_{\Delta T}} \right] |\sin \theta|^n. \end{aligned} \quad (16)$$

We note that as written,  $L/\tau$  approximates the surface velocity of the flowing glacial ice. In Figs. 8–9 we present color contour plots for the relaxation times associated with a variety of glacial structures with various values of  $H$ ,  $L$  and  $\theta$  (see Fig. 7).

Some noteworthy figures emerge. The black oval in Fig. 8 designates the e-folding relaxation time associated with a 50km long channel, sloping at  $\theta = 10^\circ$  and initiated with 200 m of glacial ice. The corresponding relaxation time is about 50 years, similar to the figure reported in Moore et al. (2016). One may interpret this timeframe equivalently as the e-folding period on which such a channel drains out a  $(1 - 1/e)$  fraction of its initial ice content. Imagining that we indeed begin with 200 m  $N_2$  thick layer and after the just described e-folding timescale, we would have remaining an ice layer of about 75 m thick which, according to Fig. 8, ought to undergo another  $(1 - 1/e)$  fractional drain in about 5000 years. Of course, this difference in drainage times is due to the strong nonlinear dependence of the mass-flux on  $H$ , namely the Arrhenius functional dependence shown in Eq. (14). Nonetheless, and all other things being equal (especially the surface temperature  $T_s$ ), any substantial amounts of ice accumulated in such drainage channels are likely to drain out to levels (say, below 50 m) in well under 100–500 years ( $\sim 0.5$ – $2$  Plutonian orbits). Similar timescale estimates can be made for structures and channels of differing extents and depths.

## 5.2. Sample initial surfaces from digital elevation models

As we are interested in the character of  $N_2$  ice flow on Pluto, we have adopted two regions along the eastern shoreline of SP to use as the topography on which the glacial ice flows. These two rectangular regions called GL-1 and GL-2, the locations with respect to SP of which are indicated in Fig. 3, are extracted from DEMs created using stereogrammetry – a method of elevation determination applied successfully in many previous studies focusing on icy satellites (Schenk, 2002; White et al., 2013). The master stereo DEM was created from 0.495 and 0.32 km/px observations<sup>7</sup> – both of which are observations obtained using the MVIC camera. The

pixel scale we adopt therefore is 0.495 km/px. The precision in relief for these DEMs is about 225 m (Moore et al., 2016).

The initial bedrock landscapes used in our simulations, shown in Fig. 10, are primed for use based on the following procedure. Because the stripped-down version of MARSSIM we use solves the equations of motion in a doubly periodic domain, the landscape should have equal elevations and gradients along the borders of the computational domain. We therefore take the raw DEM,  $Z_{\text{raw}}(x, y)$  and apply a filter which forces the elevation to be equal along the borders of the rectangular section as well as forcing the gradients there to be zero. We simultaneously impose a minimum elevation requirement at some arbitrary level  $Z_{\text{min}}$ , i.e.

$$Z_{\text{raw}} \rightarrow Z_{\text{b}} = \max[Z_{\text{raw}}, Z_{\text{min}}].$$

We always choose the elevation on the computational border to be equal to the minimum elevation  $Z_{\text{min}}$ . The resulting landscape looks like an island as can be seen in the figures. The choice of  $Z_{\text{min}}$  is guided by our desire to have some interesting topographic features appearing along the shoreline of these island-like landscapes (like, for instance, the topography indicated by red arrows on the top panel of Fig. 10). The final stage involves doubling the resolution of the model landscape using a third order spline method. This is done in order to smooth out small (pixel to pixel) scale scatter that is a byproduct of most DEM methods including stereogrammetry. Schenk (2002); White et al. (2013). The grid resolution of each of the two landscapes GL-1 and GL-2 are respectively,  $N_x \times N_y = 304 \times 340, 424 \times 452$ .

## 5.3. Some numerical results

We discuss here three suites of solutions. Each landform evolution simulation begins with a mound of  $N_2$  ice centered on at the map position  $(x, y) = (x_c, y_c)$ , with a form given by

$$H_0 = H_{r_0} \exp \left[ \left( \frac{r}{\delta r} \right)^m \right], \quad (17)$$

where  $r = \sqrt{(x - x_c)^2 + (y - y_c)^2}$ . All initial profiles use a power index  $m = 6$ . The resulting profile looks like an inverted dinner plate where ice regions close to  $r = 0$  are nearly flat with thickness  $H_{r_0}$ , while a precipitous drop off occurs at the value of  $r$  approaching the nominal mound size,  $\delta r$ . All numerical simulations adopt the non-Newtonian Arrhenius ice rheology of annealed  $N_2$  (Yamashita et al., 2010). Thus, for  $q_{\text{dry}}$ , we use the formula Eq. (14), wherein we adopt the ice surface temperatures to be  $T_s = 38.5$  K, together with  $\bar{T}_{0z} = 20$  K/km and  $T_a = 425$  K – which taken together leads to  $H_a = 0.175$  km and  $H_{\Delta T} = 1.95$  km.

Fig. 11 displays the results of a numerical simulation in which the initial  $N_2$  ice mound with  $\delta r = 4.3$  km is emplaced in the highlands of landscape GL-1 ( $x_c = 3$  km,  $y_c = -4$  km), with a very large

<sup>7</sup> Specifically, these are the P\_MPAN1 observation (resolution 0.495 km/px) and the P\_MVIC\_LORRI\_CA observation (resolution 0.32 km/px).

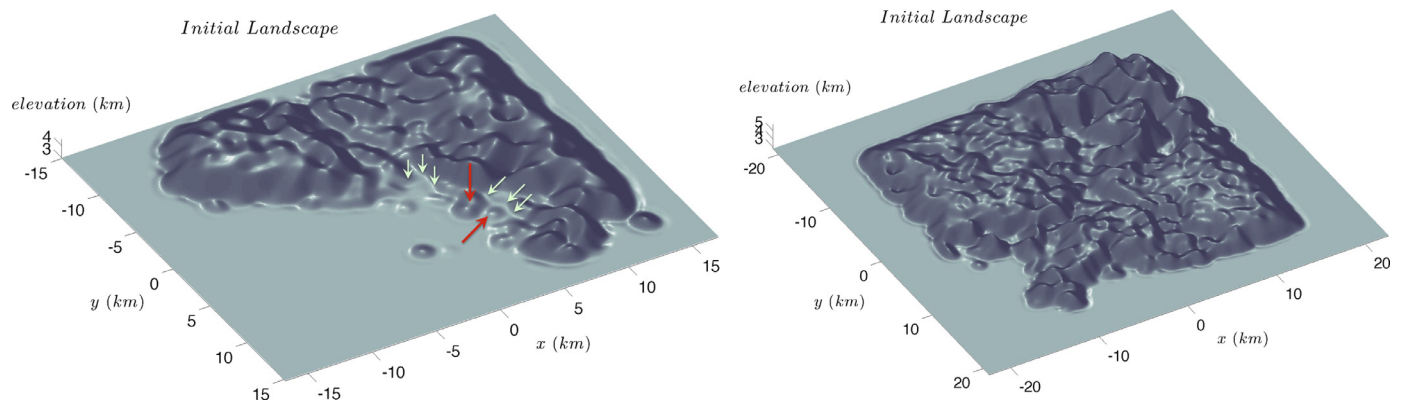


**Fig. 10.** Digital elevation models of two eastern sections of SP called GL-1 (left panel) and GL-2 (right panel). The topography has been artificially flattened along borders of frame to facilitate modeling. This surface is treated as the bedrock upon which we examine various glacial flow responses. Reference topography is indicated for GL-1: local highs (red arrows) and lows (lime arrows). This depiction of the topography simulates lighting coming from the top left of both images. (For interpretation of the references to color in this figure legend, the reader is referred to the web version of this article.)

ice thickness  $H_{r0} = 0.7$  km. Despite the large value of  $H_{r0}$ , the layer is evolved as a dry glacier (i.e. no basal melting) because the purpose of this demonstration is to exhibit how flowing glacial ice reflects bottom topography. After an initial adjustment phase of this advancing dry glacier ( $< 1$  yr),<sup>8</sup> significant ice drainage from the uplands and onto the flats occurs in under 10–20 years – both timescales which are consistent with the glacial timescale calculation in Section 5.1 as well as the numbers quoted in Moore et al. (2016).

There are several notable features in the results. Most prominently is how the ridge-line indicated by the large arrow in Fig. 10 is clearly imprinted on the surface ice once it has covered the ridgeline. The dark elongate feature in Fig. 11c, that is cut by the white transect arrow, is the expression of the aforementioned ridgeline. This elongated feature on the surface ice indicates a drop in the ice level of about 10–20 m as can be seen in Fig. 11e. Physically speaking, this drop in the ice level at the 8 km mark along this transect indicates the effect of ice piling up as it moves over and around the subsurface ridge. There are other similar elongated dark features that also similarly reflect short lengthscale changes in the bottom topography (yellow arrow). By late times,  $t = 489$  yrs Fig. 11d, this surface feature weakens because the drop in the ice level reduces the imprint to nearly imperceptible amounts.

These trends suggest that the wavy elongated features seen on the northern shores of SP, especially those seen in Fig. 2b, are not only imprints of bottom topography but are ephemeral as well. We note here that the imprint is relatively diffuse and this is likely because of the more fluid-like quality of this material due to its low value of the power law index  $n$  (see below). Nevertheless, if the wavy darkened features seen near the northern shoreline of SP are indeed imprints of topography, then this zone may have experienced a recent surge of glacial activity (in the last few hundred years). Despite the more fluid-like nature of the ice, the advancing glacial front, descending from the pitted highlands and passing through the basin and out onto the flats of the plain, is reminiscent of terrestrial glaciers that have power law indices closer to the range of  $n = 4$ –6.

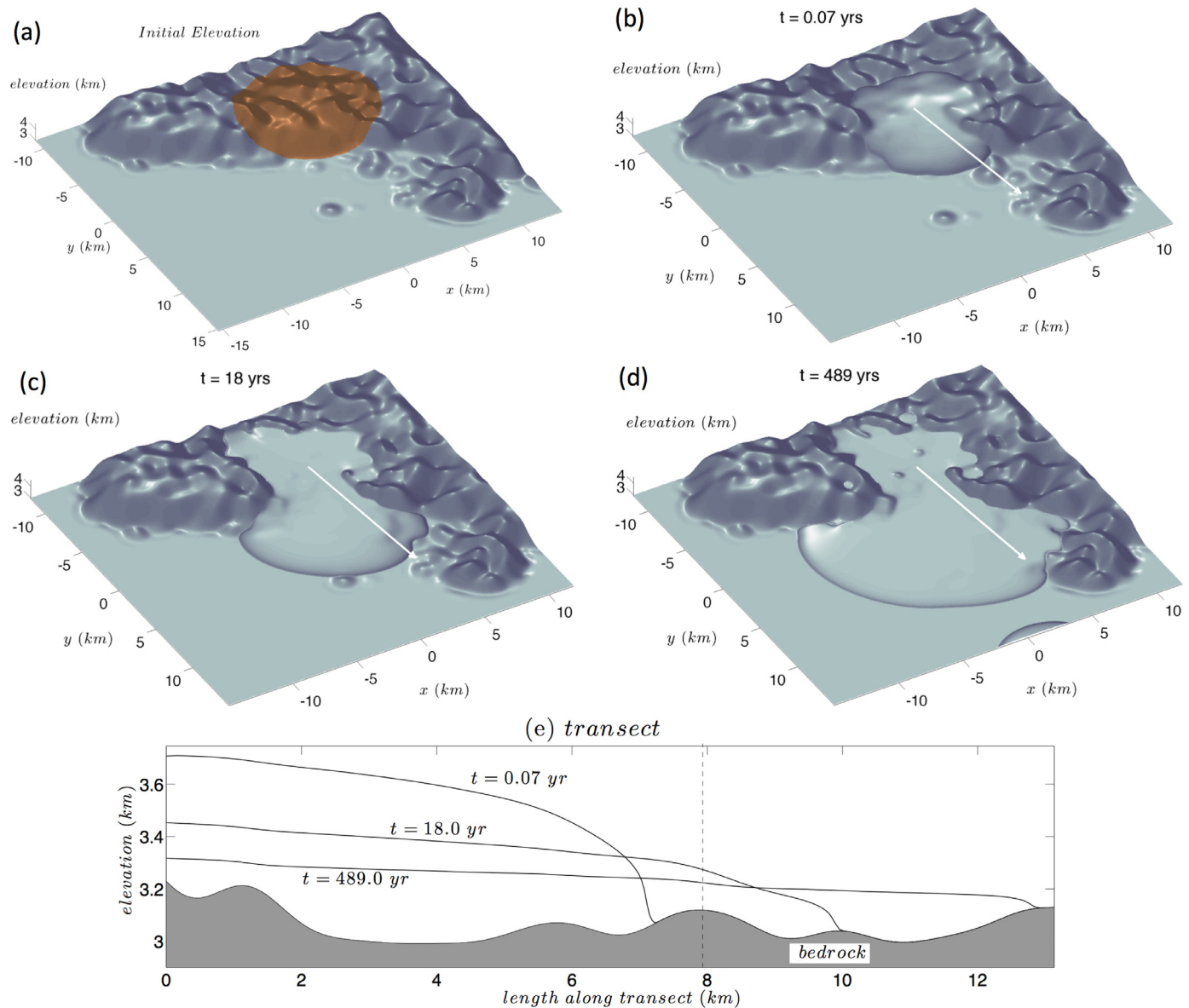
<sup>8</sup> All numerical simulations performed here have been initiated with relatively “unnatural” initial ice distributions, in the sense that they represent ice accumulations that are not those realizable from some quasi-steady process. As such, in all such cases, the simulations go through two typical stages: (i) a rapid initial readjustment phase followed by a (ii) slower creeping relaxation stage. In order to avoid numerical instabilities, this initial rapid readjustment phase must be evolved with relatively small time steps. After a sufficient amount of time in which the slowly creeping relaxation phase is reached, the time-stepping of the simulations may then be increased – generally by a factor of 5–10 times the initial time step.

Fig. 12 displays results of a similar experiment like shown in the previous figure except the original mound is placed on the flat region of landscape GL-1 ( $x_c = -2$  km,  $y_c = 4$  km) – all other parameters and conditions are otherwise the same. In this instance the flow moves toward the shoreline, yet we see similar qualitative features of topographic imprinting on the moving ice as it begins to envelope exposed relief. Interestingly, the patterning takes on a wavy character once flow begins to move into the mouth of the basin around  $x = 0$  km,  $y = 0$  km. The wavy feature reflects the local topographic low of the hills in the mouth of the basin – as pointed out by the green arrows in the left panel of Fig. 10. As before, both the wavy features eventually disappear as the  $N_2$  ice flattens out over time and the relief of the topography imprinted upon the ice is fairly muted.

By contrast, in Fig. 13 we show the result of a similar setup but with a relatively stiff rheology based on a quadri-Bingham flow model used in describing the features on the surface of Helene (Umurhan et al., 2015). The purpose of this particular demonstration is to show that the wavy features indicating bottom topography are brought out in starker relief for surface flow models with stiffer rheology. The long time fate is the same: the wavy features eventually fade over time as the surface ice relaxes. The actual properties of  $N_2$  ice rheology, possibly contaminated by other pollutants like  $CH_4$  and tholins, remain to be constrained.

We also note the persistence of the curious mesa-looking like feature in the center of the original ice mound in both Figs. 12 and 13. This is an artifact introduced by the inverted dinner-plate ice distribution. Because the center of the mound is nearly flat there is hardly any ice movement there initially. It is only when the relaxation front that proceeds from the outer rim works its way back toward the center of the mound does the flatness of the original distribution get modified. The non-circular quality at later times is an expected feature because the flat region upon which the ice mound was emplaced actually has some topography in its vicinity (see the corresponding location in the left panel of Fig. 10) – the ice flow that ensues is affected by this relief and, consequently, must move around it and locally piles up along the local subsurface relief just as one expects in classical viscous flow around an obstacle.

Fig. 14 shows comparative qualitative results involving numerical experiments of both basally wet and dry glaciers advancing on landscape GL-2. Fig. 14b-c shows the response of an initial ice mound placed on the sloping highlands of GL-2, ( $x_c = -7$  km,  $y_c = 7$  km) with  $\delta r = 4.5$  km and  $H_{r0} = 0.21$  km (Fig. 14a). Fig. 14b shows the resulting flow shape when the simulation is run for 19 years in which the glacial ice is dry. The results are very similar to



**Fig. 11.** Glacial flow evolution of dry  $N_2$  ice over landscape GL-1 with power law coefficient  $n = 2.1$  and initial mound amplitude of  $H_{i0} = 0.7$  km. Panel (a) shows initial  $N_2$  ice distribution designated by orange highlight. Panel (b) shows early readjustment of initial configuration ( $t = 0.07$  yrs). Panel (c) and (d) show the late time development of the elevation as glacial flows over topography. Flow over topography is especially pronounced over the ridgeline indicated by the red arrow in left panel of Fig. 10 and at transect position  $\sim 8.0$  km in panel (e). By late times ( $t = 489$  yrs), the drop in elevation diminishes and the imprint due to the ridgeline topography becomes increasingly imperceptible. (For interpretation of the references to color in this figure legend, the reader is referred to the web version of this article.)

the developed glacial front shown in Fig. 11. A dry glacier dynamically evolving with this value of  $n = 2.1$ , which means it leaks like a fluid down gradient, the advancing front weakly exhibits flow lobes upon reaching the flat plains.

Interestingly, Fig. 14c shows the result of the same initial configuration except for the difference that the glacial ice is allowed to be wet. In our model, a flowing glacier is considered basally wet (i.e.,  $q_{sl} \neq 0$ ), if the layer thickness of the ice  $H$  exceeds the critical value for melt at the base which, here, is when  $H > H_m = 100$  m. This number is chosen to be consistent with the depth at which melt might occur if the surface temperatures get as high as 57 K (see discussion in Section 3). Then according to Eq. (15), the base of the ice layer will slide downslope with a speed  $u_{sl0}$ , a value which we have set to 0.2 km/yr, a number adopted from basally wet glacier modeling for the Earth (Anderson et al., 2012). After 19 years, the ice has flown out onto the plains exhibiting more pronounced flow lobe structure – qualitatively reminiscent of the

lobate features observed in the New Horizons LORRI image shown in Fig. 1.

Fig. 14d shows the result of a similar simulation except the initial ice profile is centered further up the landscape ( $x_c = -3$  km,  $y_c = 3$  km), with a wider cover ( $\delta r = 9.1$  km) and with a shallower thickness ( $H_{i0} = 0.15$  km). The results are similar except that we see fast moving glacial flow reaching the flats and forming tongue-like depositional patterns below from several locations. Also, with a wider initial cover, a significant fraction of the ice rapidly infills local topographic lows. In the particular simulation shown,  $N_2$  ice is still making its way out of the pitted highlands.

## 6. Summary discussion

In this study we have developed a framework for modeling  $N_2$  glacial ice and we have used it to answer two broad qualitative questions regarding the observations of present-day glacial flow

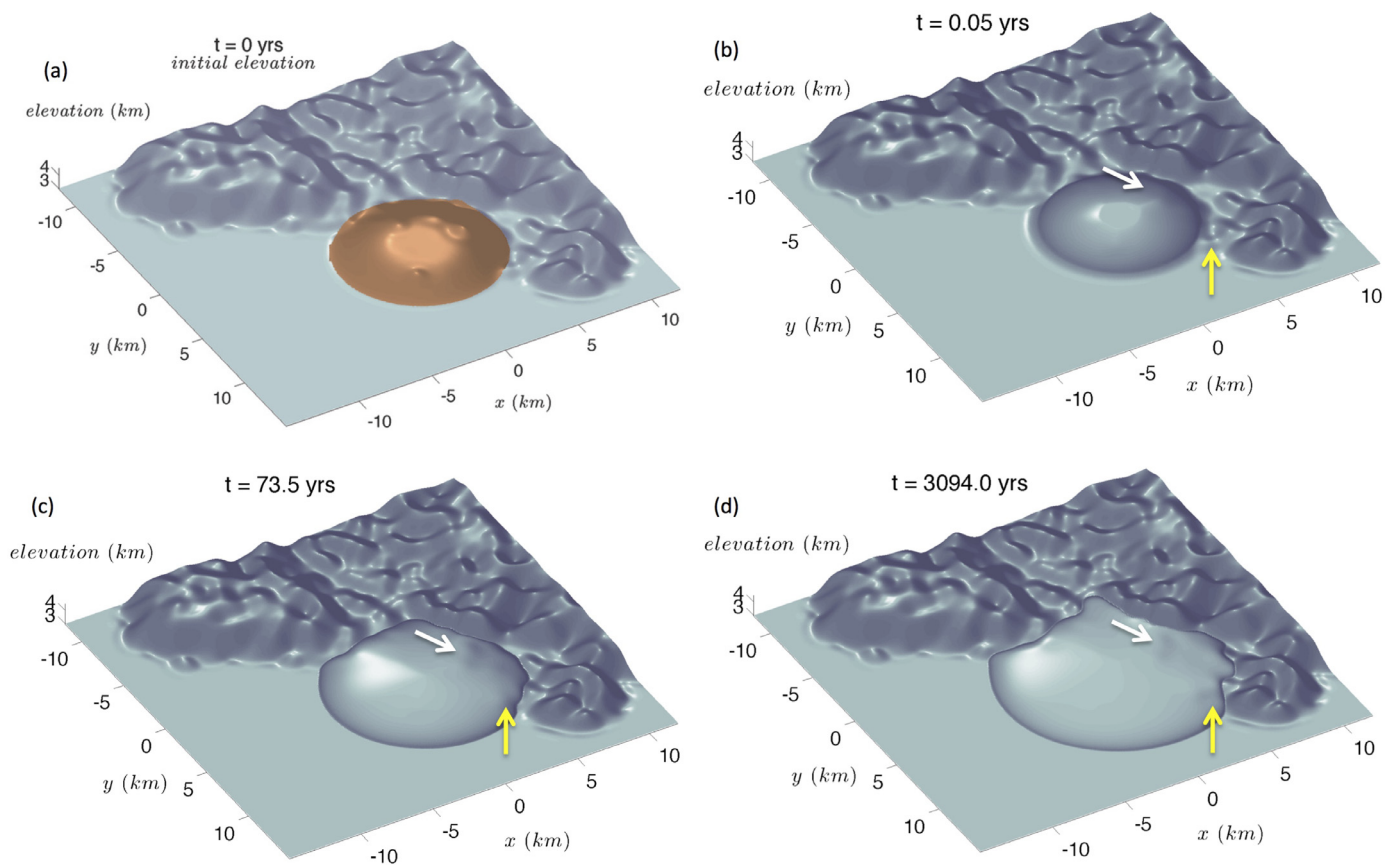


**Fig. 12.** Glacial flow evolution of dry  $N_2$  ice toward landscape GL-1. Flow parameters are  $n = 2.1$  and  $H_{st} = 1.95$  km and  $H_a = 0.175$  km with an initial mound amplitude of  $H_0 = 0.7$  km. Panel (a): Initial ice mound emplaced on flat part of bedrock (indicated by orange) is allowed to relax. Panel (b–d): early and late time configurations of this relaxation process. Topographical imprint upon the flowing glacier is apparent (white and yellow arrows). The imprint is relatively weak for this rheology. (For interpretation of the references to color in this figure legend, the reader is referred to the web version of this article.)

observed on the surface of Pluto. The glacial model incorporates the known published thermophysical properties of solid  $N_2$ . The current-day major uncertainty of the mathematical model is in the rheological properties of  $N_2$  ice under the extreme conditions of Pluto's surface. Once more laboratory and theoretical studies regarding  $N_2$ 's rheology are published, the inputs of the model developed here will need to be updated accordingly. However, the overarching mathematical framework presented here should remain largely unchanged once updates to the rheology are determined.

Our glacial flow model assumes the aspect ratio of the flowing ice is very low, which permits the development of a vertically integrated mathematical formulation (SSA). A low aspect ratio means that one may reasonably assume the ice flows laminarily. Thus, an important caveat in using this thin-layer laminar  $N_2$  flow model is the assumption that the layers are not thick enough for  $N_2$  ice to undergo convection, which would violate the assumption of laminar flow. Questions regarding onset, of course, are subject to the uncertainties in the rheology of  $N_2$  ice – a matter which needs further laboratory work to clarify.

As such and as one of the results of this work, we have analyzed the conditions for the onset of convection for a variety of basal thermal boundary conditions and find that it should occur for layers whose thicknesses are greater than 300–1000 m. This figure that depends upon the  $N_2$  ice grain diameter, whose size distribution is not currently known for the observed  $N_2$  on Pluto, although upper bounds of 1–10  $\mu$ m have been assessed from analysis of spectroscopic data taken with the LEISA instrument (Grundey et al., 2016). The thermal boundary conditions considered in our analysis include fixed-temperature conditions (traditional), fixed-

flux, and so-called planetary conditions at the base of the convecting layer. The latter two of these boundary conditions, which have not been heretofore examined in the literature in the context of solid-state convection, are meant to represent the thermo-physical conditions at the interface of a passively conducting static bedrock with an overlying  $N_2$  ice layer. We report that the conditions for onset when these latter two boundary conditions are assumed are largely similar to those assessed for the more traditional fixed-temperature basal conditions (Solomatov, 1995; McKinnon et al., 2016).

The mathematical formulation constructed here also permits the distinction between basally wet and dry glacial flow. In a work appearing in this volume (Earle et al., 2017, this volume), obliquity and orbital precession variations of Pluto can give rise to periods of time in which Pluto's surface temperature might periodically get as high as 55–60 K for 20–30 year stretches of time. Under such conditions, the base of  $N_2$  ice layers as thin as 100–200 m can melt, which would mean that one should consider a sliding  $N_2$  layer as a “basally wet glacier” (Benn and Evans, 2010; Anderson et al., 2012). While the physical manifestation of sliding  $N_2$  melt at the base of its solid ice phase has neither been observed (i.e., either in the laboratory or in images) nor considered much from a theoretical eye, it is reasonable to assume that this can happen for Plutonic  $N_2$  ices. We have both followed and implemented into our model the formulation for basally wet glacier flow used commonly in the terrestrial (water) glaciers literature, e.g., as found in Anderson et al. (2012). Given the liquid-solid phase differences between the molecules, we are cautioned from making firm statements based on the basally wet glacier runs we have reported here, although we do feel that the gross qualitative trends seen in our simulations

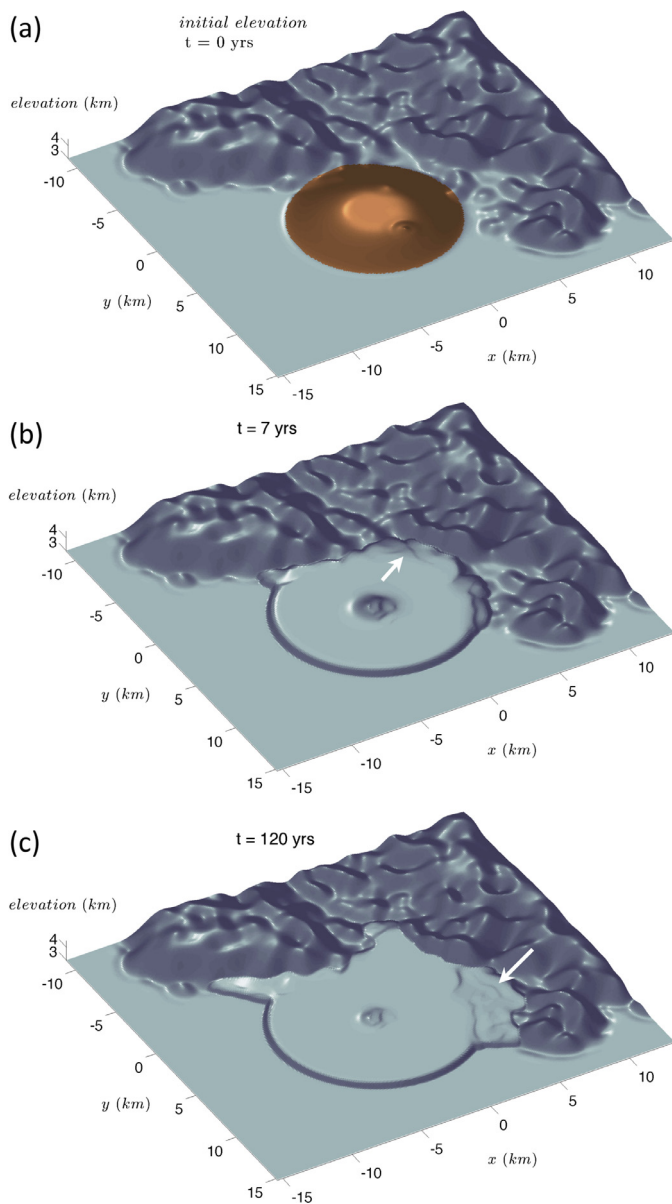


**Fig. 13.** Glacial flow evolution of dry  $N_2$  ice toward landscape GL-1. Similar numerical experiment to Fig. 12 except for a stiffer rheology (see text). Panel (b-c): early and late time configurations of this relaxation process. Note the appearance of wavy patterns (white arrows) and their qualitative resemblance to similar undulating patterns seen near the northern shore of SP (Fig. 2). Wavy patterning is an imprint of local topographic extremes shown by the green arrows in the left panel of Fig. 10. The wavy pattern indicated by arrow in panel (b) is no longer visible at later times, panel (c). (For interpretation of the references to color in this figure legend, the reader is referred to the web version of this article.)

are likely to be robust. As such, when laboratory investigations relevant to both wet and basally wet  $N_2$  glaciers are performed in the future, their results should inform upon improvements to the way in which such sliding masses are modeled and, moreover, much of the basally wet glacier simulations reported here ought to be redone.

The vertically integrated glacial flow has a dry mass-flux form that is similar to the more familiar Glen-law formulation, which has a power law dependence with layer thickness, i.e.,  $\sim H^{n+2}$ . However, based on the strongly insulating nature of  $N_2$  ice, we find that the mass-flux formulation deviates from this more traditional form and instead has (what we have here called) an “Arrhenius-Glen” form in which the layer thickness dependence of the mass-flux coefficient is as follows

$$\sim H^{n+2} \exp \left[ \frac{H/H_a}{1 + H/H_{\Delta T}} \right],$$

where the parameters  $H_a$  and  $H_{\Delta T}$  depend upon the activation energy of  $N_2$  ice, the surface temperature of the glacier, and the geothermal flux emerging from the interior of the planet. We are cautioned by noting that future improvements in the knowledge of  $N_2$  ice rheology will likely require reconsideration of the mathematical forms and timescales we have presented in this study.

We have applied this model to qualitatively answer the two questions we have posed in the introduction:

1. The wavy transverse light-dark patterning very near the northern shore of SP (Fig. 2a-b) has been interpreted by us to be evidence of glacial flow from the center of SP toward the shoreline (Howard et al., 2017, this volume). Is the pattern a result of northward advection downwelling zones of convecting  $N_2$  ice or are they imprints of the bottom topography present not too far beneath under the surface? We find from our simulations that it is likely that the features are steps in the flowing  $N_2$  ice tracing out locations of bottom topography. In many simulations that we have run, the darkened features correspond to 10–20 m step drops in the ice level as it passes over the peak of the bottom topography. If the surface ice on Pluto is characterized somehow by a stiffer rheology, perhaps due to contaminants like small  $CH_4$  grains, our simulations indicate that the imprint of bottom topography is more dramatic. Given the currently poor constraints on  $N_2$  ice (and its mixtures), we consider this possibility as not being necessarily ruled out. For stiffer rheologies, the wavy patterns appearing on the surface of the modeled ice can be an indicator of localized lows in the bottom topography. In either case of stiff or non-stiff rheologies, the features are ephemeral as they eventually fade away on time scales approaching a few decades to hundreds of years. If indeed the wavy patterning seen near the northern shoreline of SP is an indicator of bottom topography, then it is reasonable to suggest that this part of SP has recently experienced a surge of northward flow within the last two centuries – perhaps even as recently as in the last few decades.
2. The dark lobate depositional features seen on the eastern shoreline of SP (Fig. 1) are another strong line of evidence pointing at recent glacial flow activity. Fig. 1 shows such glacial flow emanating from the pitted highlands of ETR and onto the flats below. Were the glacial flow events responsible for these and similar features a result of dry or basally wet glacial flow? Our simulations suggest that it is very hard to get very pronounced tongue-like lobate features of down-flowing glacial ice if it moves strictly as a dry glacier with a power-law index  $n$  around 2. In the simulations we have reported here, the advancing dry glaciers generally form weakly lobate fronts. However, if the base of the glacial ice is wet, then it drains out onto the flats below, exhibiting unmistakably pronounced lobate features like pointed out in Fig. 14c-d.

We are not implying that all  $N_2$  glacial ice that drains into SP from the pitted highlands surrounding SP does so as a wet or basally wet glacier. However, based on the obliquity-eccentricity variations experienced by Pluto, we consider it perhaps possible that there may have been episodes of rapid drainage of the  $N_2$  ice found in the pitted highlands of ETR and into SP when the surface temperatures get high enough, since it would mean basal melt  $N_2$  ice can occur for shallower layer thicknesses. In other words,  $N_2$  ice which would have otherwise emptied into SP’s basin as a dry glacier may have rapidly drained into the basin as a basally wet glacier during these brief periods of surface warming. As a basally wet glacier, then, they could be the origins of the tongue-like lobate features observed on today’s surface. Of course, we caution that

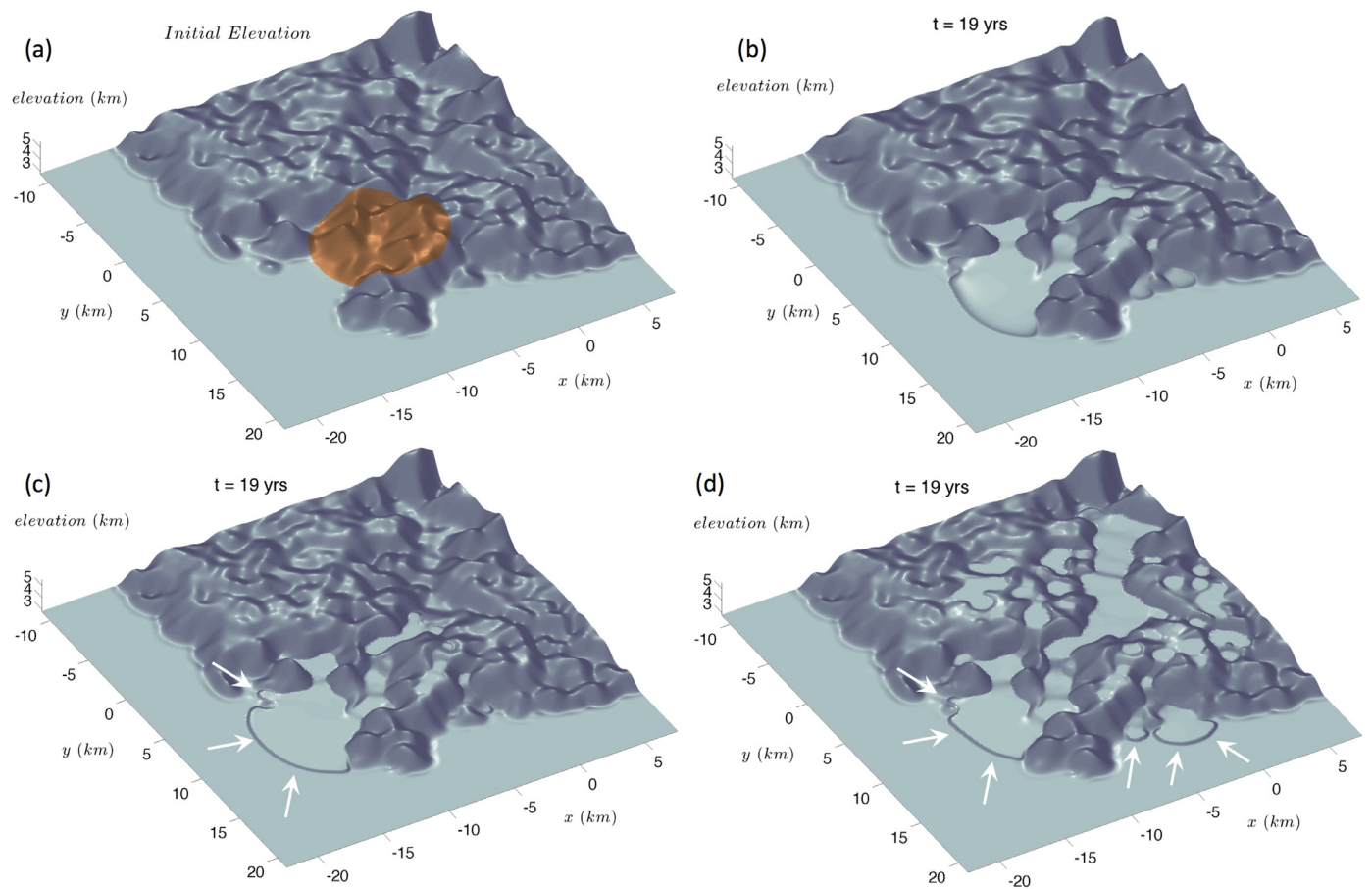


**Fig. 14.** Glacial flow evolution over landscape GL-2 of either basally wet or dry  $N_2$  ice with  $n = 2.1$  and  $H_{\Delta r} = 1.95$  km and  $H_a = 0.175$  km and initial mound amplitude of  $H_0 = 0.21$  km. Panel (a) exhibits the initial ice mound emplaced on sloping highlands which is then allowed to relax. The resulting shape after 19 years is shown for the case of no basal slip, panel (b); and with basal slip, panel (c). In the latter - slip occurs with a speed  $u_{00} = 0.2$  km/yr once the local ice layer thickness exceeds  $H > H_m = 100$  m. Panel (d) depicts a similar numerical experiment involving basally wet glacial flow, but for a wider shallower initial ice mound (details in text). Owing to the relatively low power law index, simulations of both of basally wet and dry glacial flow develop classical flow lobe features once ice has reached the flats. Flow lobes are more pronounced in basally wet flow simulations. The numerical experiment in panel (d) shows how glacial ice collects inside local topographic lows as well.

these hypothetical possibilities have not yet been assessed to their fullest.

The questions posed and the answers given in this study are very preliminary. When the rheology of  $N_2$  ice, both as a pure substance as well as an ice comprised as a mixture of other volatile grains like  $CH_4$  and  $CO$ , most of the simulations and questions examined here must be revisited. Similarly, there are many more questions to be answered at this early stage of discovery. The qualitative ones we have addressed here give us confidence that the glacial model we have developed may be used to answer more detailed and refined questions once more data analysis of Pluto's surface is complete. One of the next directions is to apply the machinery developed here to answer questions about Pluto's past glaciation (Howard et al., 2017, this volume).

### Acknowledgments

The corresponding author thanks Magda Saina for assistance with some of the figures presented here. The authors thank both the anonymous referee as well as Dr. D. A. Patthoff for very helpful suggestions that helped to streamline this work. The authors are also indebted to Dr. W. Grundy for spirited conversations regarding the granular nature of Pluto's surface ices. This work was supported by both NASA's Senior NPP program and NASA's New Horizons project.

### Appendix A. On the dominance of NH-creep over Coble creep

Volume (NH) and boundary (Coble) diffusional creep mechanisms are (respectively) represented in sum as

$$\dot{\epsilon} = \dot{\epsilon}_v + \dot{\epsilon}_b, \quad (\text{A.1})$$

in which

$$\dot{\epsilon}_v = \frac{42D_{0v}\Omega\sigma}{kTd_g^2} e^{-E_v/kT}, \quad (\text{A.2})$$

$$\dot{\epsilon}_b = \frac{42D_{0b}(2\pi\delta)\Omega\sigma}{kTd_g^3} e^{-E_b/kT}, \quad (\text{A.3})$$

where  $E_v$ ,  $E_b$  are the associated activation energies,  $D_{0v}$ ,  $D_{0b}$  are the measured reference diffusion rates,  $d_g$  is grain size,  $\Omega = 4.7 \times 10^{-29}$  m<sup>3</sup> is the volume of a single  $N_2$  molecule. The second invariant of the stress-tensor is  $\sigma$ . In Coble creep the quantity  $2\pi\delta$  is a measure of the width of the grain boundary through which molecules diffuse and this is assumed to be a few widths of a volume of a single  $N_2$  molecule – thus we take  $\delta \approx \Omega^{1/3}$ . Laboratory measurements of only volume diffusion parameters (i.e.,  $D_{0v} = 1.6 \times 10^{-7}$  m<sup>2</sup>/s and  $E_v = 8.6$  kJ/mole) are available as of the writing of this manuscript. In lieu of these parameters for Coble creep we follow (Eluszkiewicz and Stevenson, 1990; Eluszkiewicz, 1991) who assume that  $D_{0b} = D_{0v}$ , while also assuming  $E_b = (2/3)E_v$ , the latter being a suggestion made originally in Ashby and Verall (1978). The activation energies may be expressed in terms

of activation temperatures respectively as  $T_v \equiv E_v/k = 1033$  K and  $T_a \equiv E_b/k = (2/3)E_v/k = 686$  K. The point at which the two creep rates are equal defines a relationship between temperature and grain size beyond which NH creep will dominate over Coble creep. Thus, setting  $\dot{\epsilon}_v = \dot{\epsilon}_b$  and sorting through the algebra reveals that the critical temperature for this transition ( $T_{cc}$ ) occurs when

$$T_{cc} = T_b \cdot \frac{1}{\ln(d_g/2\pi\Omega^{1/3})}. \quad (\text{A.4})$$

For a  $N_2$  grain of size 1mm,  $T_{cc} = 24$  K. Thus, given the aforementioned experimental uncertainties, this means under Pluto's current surface conditions NH creep is likely to be the dominant operating creep mechanism provided the tangential stresses are well below the power-law regime, a figure currently not well constrained ( $< 0.001$ –1 MPa).

## Appendix B. Infinite Prandtl-number equations

The linearized non-dimensional 2D equations describing the onset of convection in infinite-Prandtl number media is given by

$$0 = -\nabla\Pi + Ra\Theta\hat{\mathbf{z}} + \nabla \cdot \nu\nabla\mathbf{u} \quad (\text{B.1})$$

$$\partial_t\Theta - w = \nabla^2\Theta \quad (\text{B.2})$$

$$\partial_x u + \partial_z w = 0. \quad (\text{B.3})$$

Length and horizontal space dimensions  $x$  and  $z$  are scaled by the layer thickness  $H$ , velocity scales are scaled by  $\kappa/H$ , while time-scales are given by  $\kappa/H^2$ . The quantity  $\Theta$  represents the deviations from the static conductive temperature profile, i.e.,  $T(z, z, t) = T_s + \Delta T\Theta - \bar{T}_{oz}z$ , in which  $\Delta T = H\bar{T}_{oz}$ . The Rayleigh number at the base is given as

$$Ra \equiv 1.13 \times 10^{13} \left(\frac{H}{\text{km}}\right)^4 \left(\frac{d_g}{\text{mm}}\right)^{-2} \times \exp\left(-\frac{T_a}{T_b}\right) \left(\frac{\bar{T}_{oz}}{\bar{T}_{oz}^{(ref)}}\right), \quad (\text{B.4})$$

where the reference temperature gradient we adopt is  $\bar{T}_{oz}^{(ref)} = 20$  K/km, the base temperature  $T_b \equiv T_s + H\bar{T}_{oz}$  and the activation temperature  $T_a = 1030$  K. We set the surface position  $z_s = 0$ . The function  $\nu$  is the viscosity scaled by the viscosity at the bottom of the layer and is an explicit function of the height parameter  $z$  and whose exact form here is

$$\nu = \exp\left[\frac{T_a}{T_s - z\bar{T}_{oz}} - \frac{T_a}{T_b}\right]$$

However, to facilitate calculation we adopt for  $\nu$  the Frank-Kamenskii approximation, e.g. [Solomatov \(2012\)](#), which replaces the Arrhenius form above with a simple exponential, i.e.,

$$\nu = e^{pz}. \quad (\text{B.5})$$

Consequently we identify  $\ln p$  as equivalent to the ratio of  $\nu_t/\nu_b$ , the ratio of the top viscosity to the bottom viscosity. This approximation works well when the viscosity differences become greater than a factor of 1. A more detailed calculation utilizing the correct Arrhenius form will be reserved for a future calculation.

We assume a streamfunction formulation for the incompressible perturbation velocity field, i.e.,  $u = -\partial_z\psi$  and  $w = \partial_x\psi$ , and we assume steady solutions of the form

$$\Theta(x, z) = \Theta_k(z)e^{ikx} + c.c. \quad (\text{B.6})$$

and similarly for the streamfunction  $\psi$ . The horizontal wavenumber is  $k \geq 0$  and the vertical eigenfunctions  $\Theta_k(z)$ ,  $\psi_k(z)$  are associated with each wavenumber  $k$ .

For kinematic boundary conditions we employ rigid conditions at the bottom boundary  $z = 0$ ,  $u = w = 0$  and stress-free, no-normal flow at  $z = 1$ ,  $w = \partial_z u = 0$ . Owing to the fact that the surface of Pluto today is in vapor pressure equilibrium, we consider it reasonable to impose fixed temperature boundary conditions at the top. This means that  $T(z = 1) = T_s$ , which translates to  $\Theta = 0$  at  $z = 1$ . The bottom thermal condition, on the other hand, is less clear. If the bottom ice layer interfaces with an active liquid layer (as in solid-state convection models of Enceledus and Europa) then it is reasonable to fix the bottom temperature of the ice layer to the temperature of the top of the liquid layer, which here effectively translates to  $\Theta = 0$  at  $z = 0$ , and henceforth we refer to these as *fixed-temperature* boundary conditions.

However, if the substrate is a static  $H_2O$  ice “bedrock”, then the correct boundary conditions become less clear and several options offer themselves here. The substrate presumably passively conducts the geothermal flux emanating from the interior of Pluto and, as such, imposing so-called *fixed-flux* boundary conditions is reasonable, in which  $\partial_z T = -\bar{T}_{oz}$  which translates to  $\partial_z \Theta = 0$  at  $z = 0$ . Perhaps, a more physically accurate model is to suppose that the  $H_2O$  ice bedrock thermally adjusts to the temperature fluctuations taking place in the convecting ice-layer above. Then following the methodology of [Hurle et al. \(1967\)](#) we match solutions in the convecting ice-layer onto solutions within the static  $H_2O$  ice bedrock. As we noted in [Section 2.1](#) the thermal conductivity of  $H_2O$  ice is nearly 20 times that of  $N_2$  ice, i.e.,  $K_{H_2O} \approx 20K_{N_2}$ . Then according to the procedure outlined in [Sparrow et al. \(1964\)](#); [Hurle et al. \(1967\)](#) the bottom boundary condition, in a calculation examining the conditions of onset (i.e.,  $\partial_t \rightarrow 0$ ), means imposing

$$\partial_z \Theta_k|_{z=0} = k\Theta_k|_{z=0} (K_{H_2O}/K_{N_2}), \quad (\text{B.7})$$

for every horizontal wavenumber  $k$ . We refer to these thermal conditions as *planetary*.

The solution method follows basic procedures, e.g., see [Chandrasekhar \(1961\)](#), except for the fact that the critical values of  $Ra$  and corresponding eigenfunctions must be assessed numerically. We solve the resulting one dimensional sixth order system on a Chebyshev grid using standard matrix inversion methods found in all Matlab packages. We have verified the robustness of the solutions by comparing the expected critical  $Ra$  number for conditions in which the viscosity is constant. In the instance when both bottom and top thermal boundary conditions are fixed-temperature, together with rigid conditions at the base and

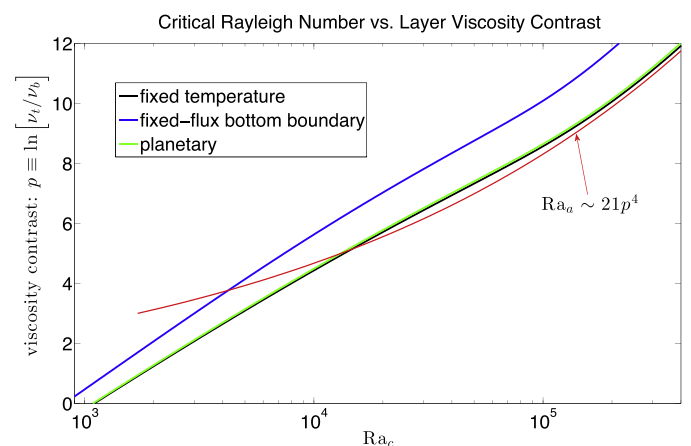


**Fig. B.15.** Critical value of the basal  $Ra$  versus viscosity contrast  $p$  for the onset of solid-state convection in  $N_2$  ice for parameters shown in [Fig. 5](#). Results for three different boundary conditions are displayed. The asymptotic relationship  $Ra_c \approx Ra_a = 21p^4$  is indicated by the red curve. (For interpretation of the references to color in this figure legend, the reader is referred to the web version of this article.)

stress-free conditions at the top, the transition  $Ra = 1101$ . Our methods exactly reproduce this value in that case.

We show in Fig. B.15 the corresponding critical values of the base  $Ra$  ( $Ra_c$ ) against the value of the viscosity contrast  $p$  for the three different thermal boundary conditions described. We also show the asymptotic value of  $Ra_c \approx Ra_a = 21p^4$  which is appropriate for temperature dependent Newtonian convection with fixed-temperature boundary conditions at both boundaries (Solomatov, 1995).

### Appendix C. Glacial model development

The details of the glacial flow model is presented here.

#### C.1. Modeling framework

As we examined in Section 2.2, glacial ice is assumed to have a stress-strain rate relationship of the following generic form  $\dot{\epsilon} = A\sigma^n$ , where  $A = A(T)$  and  $n = n(T)$ , and where  $\sigma$  is the local material stress which is a function of depth from the surface. Using Fig. 7 as a reference, we see that if the gradient of the local surface slopes with a magnitude angle  $\theta$  with respect to the horizontal, then the corresponding magnitude of the instantaneous stress is given by  $\sigma = \rho_s g(z_s - z) \sin \theta$  where, as before,  $z_s$  is the height of the local surface located on the map coordinates  $x, y$ , i.e.  $z_s = Z(x, y, t)$  over time  $t$ . The angle  $\theta$  is given by

$$\sin \theta = S/(1 + S^2)^{1/2}, \quad S \equiv |\nabla Z| = |\tan \theta|. \quad (C.1)$$

In the limit of vanishingly small aspect ratios of (nearly) incompressible flowing materials, it is a fair assumption to approximate the resulting flow as being purely horizontal with no vertical component of velocity. As such, we assume we are in a regime in which SSA is valid. As such, the model procedure in the SSA converts the generic stress-strain relationship into a vertically varying horizontal flow field vector equation, i.e.,

$$\begin{aligned} \frac{\partial \mathbf{u}}{\partial z} &= A[\rho_s g(Z - z)]^n (\sin \theta)^{n-1} \cos \theta \nabla Z \\ &= A[\rho_s g(Z - z)]^n \frac{S^{n-1}}{(1 + S^2)^{n/2}} \nabla Z. \end{aligned} \quad (C.2)$$

where the horizontal velocity vector is related to its component velocities via the relationship  $\mathbf{u} = u(x, y, t)\hat{\mathbf{x}} + v(x, y, t)\hat{\mathbf{y}}$ .

The procedure continues by integrating Eq. (C.2) once to solve for  $\mathbf{u}(x, y, t)$ , subject to a basal boundary condition. If the ice has not melted (henceforth “dry”), then we assume rigid boundary conditions and assign  $\mathbf{u} = 0$  at the base of the layer  $z = Z_b(x, y, t) \equiv Z - H$ , where  $H = H(x, y, t)$  measures the thickness of the ice-layer. Thus

$$\begin{aligned} \mathbf{u}(x, y, z, t) &= \mathbf{u}_{\text{dry}}(x, y, z, t), \\ \mathbf{u}_{\text{dry}} &\equiv \int_{Z_b}^z A[\rho_s g(Z - z')]^n \frac{S^{n-1}}{(1 + S^2)^{n/2}} \nabla Z dz' \end{aligned}$$

We often will be interested in diagnosing the surface velocities of the flowing ice which we define by  $\mathbf{U}(x, y, t) \equiv \mathbf{u}(x, y, Z, t)$ .

Given today’s surface temperatures of Pluto ( $\sim 38.5$  K), and unless the predominant diameter of  $N_2$  ice grains is much larger than a few millimeters, it is difficult to get basal melt of  $N_2$  before the onset of convection inside a layer. However, as discussed in Earle et al. (2017, this volume) and reviewed in Section 2.4, it is possible that the surface temperatures of Pluto’s  $N_2$  ices get high enough so that the base of a  $N_2$  ice layer will exceed its triple point. While the physical properties of  $N_2$  ice glaciers with basal melt represents a wholly new subject matter in which very little is known both experimentally and theoretically, we consider including this possibility in our models using very general considerations borrowed from the literature of terrestrial  $H_2O$  ice glaciers. Following

Anderson et al. (2012), we suppose that the base of a  $N_2$  ice layer will slide with a constant (prescribed) velocity,  $\mathbf{u}_{\text{sl}}$  in a direction prescribed by the gradient of the ice surface and only if the depth and basal temperatures exceed the minimum required for  $N_2$  melt. Thus, we write

$$\mathbf{u}_{\text{sl}} = \begin{cases} u_{\text{sl}} \hat{\mathbf{t}}, & H > H_m, \\ \mathbf{0}, & 0 < H < H_m, \end{cases} \quad (C.3)$$

in which the map-directional vector  $\hat{\mathbf{t}} \equiv \nabla Z/|\nabla Z|$ .  $u_{\text{sl}}$  is the speed of the basal flow which is a model input parameter, possibly a function of other inputs. The minimum ice-thickness quantity  $H_m$  is a model that takes into account the aforementioned requirements of depth (normal to the ice-layer surface) and surface temperature  $T_s$ . For the models examined in this study we will adopt constant values for these quantities, keeping in mind that matters become far more nuanced and complicated when more physical realism is the aim,<sup>9</sup> a goal that will be addressed in future follow-up studies. Nonetheless, in the event that basal melt happens, then the flow velocity field is basally wet, which means it is written as a sum of the dry-field plus the sliding due to basal melt, i.e.,

$$\mathbf{u} = \mathbf{u}_{\text{dry}} + \mathbf{u}_{\text{sl}}. \quad (C.4)$$

The penultimate stage in developing the model involves the formulation of a mass-flux rate  $\mathbf{q}$ , defined as a second integral over the ice-layer of mass flux  $\rho_s \mathbf{u}$ , i.e.,

$$\mathbf{Q}(x, y, t) \equiv \int_{Z_b}^z \rho_s \mathbf{u} dz = Q_0 \nabla Z, \quad (C.5)$$

where the mass-flux scalar prefactor is

$$Q_0 = Q_0(Z_b, H, T_s, T_b, n, \dots),$$

in which  $T_b$  is the base temperature of the ice-layer. We explicitly consider the contribution of the mass-flux due to whether or not basal melt is included. This is to say that we identify individual contributions to the mass flux,  $\mathbf{Q} = \mathbf{Q}_{\text{sl}} + \mathbf{Q}_{\text{dry}}$ , as being a sum derived from basal melt and dry flow. The former of these is

$$\mathbf{Q}_{\text{sl}} = \rho_s H \mathbf{u}_{\text{sl}} = \rho_s H \begin{cases} u_{\text{sl}} \hat{\mathbf{t}}, & H > H_m, \\ \mathbf{0}, & 0 < H < H_m, \end{cases} \quad (C.6)$$

Below in Section C.2 we explicitly examine the form of the dry component of the mass flux  $\mathbf{Q}_{\text{dry}}$ , as well as the difficulties it admits.

We add the following ingredients: We permit the possibility of a steady form of sublimation/deposition from/onto the surface which we denote by  $\dot{H}_a$ . Surface sublimation/deposition is assumed to occur at a uniform rate in the direction of the local surface normal – a formulation used in previous landform evolution models e.g., Howard (2007); Howard et al. (2012). However we are sensitive to the fact that the true amount of deposition/sublimation is a function of the surface temperatures of the atmosphere, as well as the  $N_2/CO$  vapor content of the atmosphere wherein these quantities are, in turn, functions of Pluto’s location on its orbit. Despite these caveats, we think it fair to consider this more simpler formulation

<sup>9</sup> There are many shortcomings of this initial model prescription that ought to be rectified in future modeling. Some of these issues include the following: The first, and probably most important, is the way that mixing of melted  $N_2$  is handled. Liquid  $N_2$  is 20% more buoyant than its solid phase, and so the matter of the quality (is it a slush?) and timescale of vertical mixing of liquid  $N_2$  into its solid phase must be addressed in a future detailed physical study. Another matter is the lack of accounting for the bottom topography at the ice-bedrock interface which can, in fact, hinder or alter the ability of the basally melted layer to move at all if, for instance, the bedrock shape is locally upwardly convex which would imply the emergence of a trapped pool/lake of liquid  $N_2$  on the bedrock and lying underneath a covering of solid  $N_2$ . Until the level of the liquid phase reaches the brim of the bedrock bowl, one does not expect net flow due to basal melt. The model as presented here does not distinguish this subtlety.

to investigate the various physical manifestations of basic glacial flow on Pluto's surface. More sophisticated modeling is reserved for future studies.

Additionally, we permit the possibility that a certain amount of the substrate bedrock may be eroded by the moving ice through the processes of scouring or plucking (e.g., Anderson et al., 2012) and subsequently absorbed into it and carried along.<sup>10</sup> We represent this erosion/incision rate by  $\dot{Z}_b$  and allow for the possibility that it is strictly a function of (i) the total stress exerted at the glacier/bedrock interface if there is no basal melt, (ii) glacial ice sliding speeds if there is basal melt and, possibly, (iii) the total "traffic" of moving ice, defined as  $|\mathbf{q}|$ . Thus, the complete set equations of motion are

$$\partial_t Z = \nabla \cdot \mathbf{q} + \dot{H}_a + \dot{H}_b, \quad (\text{C.7})$$

$$\partial_t Z_b = -\dot{H}_b, \quad (\text{C.8})$$

in which  $\mathbf{q} \equiv \mathbf{Q}/\rho_s$  with  $q_0 \equiv Q_0/\rho_s$  together where  $\mathbf{Q}$  is given in Eq. (C.5). Because we treat the density as nearly constant, we prefer to follow the rate of change of the local elevation  $Z$  instead of the mass-flux rate of change, which is why we have opted to work with the flux quantity  $\mathbf{q}$ .

## C.2. Approximate form for dry ice mass-flux and velocities

We examine the form of the velocity fields and corresponding mass-flux in a scenario where there is no basal melt. In the event that both  $A$  and  $n$  are independent of depth  $z$ , then the dry component of  $q_0$  may be evaluated analytically, in which case we say

$$q_0 \rightarrow q_{\text{glen}} \equiv A_c (\rho_s g)^n \frac{H^{n+2}}{n+2} \frac{S^{n-1}}{(1+S^2)^{n/2}}, \quad (\text{C.9})$$

recovering the familiar Glen law form (Glen, 1955; Benn and Evans, 2010; Umurhan et al., 2015). Also in this limiting case we can exactly assess both the horizontal velocity field of the dry  $\text{N}_2$  ice,

$$\begin{aligned} \mathbf{u}(x, y, z, t) &\rightarrow \mathbf{u}^{(c)}(x, y, z, t) \\ &= \frac{A_c H}{n+1} (\rho_s g H)^n \left[ 1 - \left( \frac{Z-z}{H} \right)^{n+1} \right] \frac{S^{n-1} \nabla Z}{(1+S^2)^{n/2}}, \end{aligned} \quad (\text{C.10})$$

and similarly the surface velocity of the dry flowing ice, i.e.,

$$\mathbf{U}(x, y, t) \rightarrow \mathbf{U}^{(c)}(x, y, t) = \frac{A_c H}{n+1} (\rho_s g H)^n \frac{S^{n-1} \nabla Z}{(1+S^2)^{n/2}}, \quad (\text{C.11})$$

where the superscript "(c)" denotes the corresponding expression for constant values of  $A = A_c$  and  $n$ . For the following comparative analysis, it is useful to rewrite the velocity field as a product of two functions

$$\mathbf{u}^{(c)}(x, y, z, t) = \mathbf{U}^{(c)}(x, y, t) \cdot \Xi^{(c)}(z), \quad (\text{C.12})$$

$$\Xi^{(c)}(z) \equiv 1 - \left( \frac{Z-z}{H} \right)^{n+1}. \quad (\text{C.13})$$

$\text{N}_2$  ice rheologies have temperature dependencies, namely in the pre-factor  $A$  and stress-strain exponent  $n$ . Given our earlier remarks in Sections 2.3 and 3, and assuming the ice-layers under consideration are not undergoing convection, the interior temperatures increase linearly with depth which makes writing down clean formulae for  $Q_0$ ,  $\mathbf{u}$  and  $\mathbf{U}$ , as in Eqs. (C.9)–(C.11), unwieldy in most cases – especially when  $A$  is characterized as an Arrhenius

function of temperature. Nonetheless, to clarify matters and help motivate a useful approximate form, we express the exact solution for  $\mathbf{u}$  as a similar product of two functions, i.e.

$$\mathbf{u} \equiv \mathbf{U}^{(c)} \Xi(z), \quad (\text{C.14})$$

where we evaluate  $A_c \rightarrow A_s = A(T = T_s) = A(z = Z)$  and letting

$$\Xi(z) \equiv (n+1) \int_{\zeta_b}^{\zeta} \frac{A(\zeta')}{A_s} \left( \frac{Z}{H} - \zeta' \right) d\zeta', \quad (\text{C.15})$$

$$\zeta \equiv z/H, \quad \zeta_b \equiv Z_b/H. \quad (\text{C.16})$$

Our goal then is to develop an approximate solution,  $\Xi^{(\text{approx})}$ , for the exact vertical structure function  $\Xi(z)$  – the latter of which must be determined numerically.

We are reminded that the index  $n$  weakly varies with respect to temperature based on the laboratory annealed  $\text{N}_2$  experiments of Yamashita et al. (2010), viz. Section 2.2, and that the strongest variations will arise due to the temperature dependence of  $A$ . A practical strategy then to handle this is to adopt a constant value of  $n$  and consider two end-state values of  $A$ : one corresponding to its value based on the surface temperature and one based on the temperature at the base of the layer. In other words, one proceeds by adopting the forms for  $Q_0$ ,  $\mathbf{u}$  and  $\mathbf{U}$  given in Eqs. (C.9)–(C.11) but replacing  $A_c$  with  $A_s = A(T_s)$  for the upper end-state and the other lower-end state by replacing  $A$  with  $A_b = A(T_b)$  where  $T_b$  is the bedrock temperature as discussed in Section 3. We consider two choices for the approximate vertical structure function form  $\Xi^{(\text{approx})}$ : one is where one sets  $A(\zeta') \rightarrow A_s$  in the definition found in Eq. (C.15), i.e.

$$\Xi^{(s)} = (n+1) \int_{\zeta_b}^{\zeta} \left( \frac{Z}{H} - \zeta' \right) d\zeta' = \Xi^{(c)}, \quad (\text{C.17})$$

and the second one is  $A(\zeta') \rightarrow A_b$

$$\Xi^{(b)} = (n+1) (A_b/A_s) \int_{\zeta_b}^{\zeta} \left( \frac{Z}{H} - \zeta' \right) d\zeta' = \exp \left[ \frac{H/H_a}{1+H/H_{\Delta T}} \right] \Xi^{(c)}, \quad (\text{C.18})$$

in which the ratio  $A_b/A_s$  was evaluated assuming the generic Arrhenius functional forms posited in Section 2.2. The quantities appearing are  $H_{\Delta T} \equiv T_s/\bar{T}_{0z}$  and  $H_a \equiv T_s^2/T_a \bar{T}_{0z} = H_{\Delta T} \cdot (T_s/T_a)$ . We consider a third possibility, which is similar to  $\Xi^{(b)}$  except it is multiplied by a corrective factor  $g_q$  chosen to produce an exact scalar equivalence between the exact mass flux and this approximate form. Thus, we also consider

$$\begin{aligned} \Xi^{(q)} &= g_q \Xi^{(b)} \\ g_q &= \int_{\zeta_b}^{Z/H} \Xi(\zeta) d\zeta \Big/ \int_{\zeta_b}^{Z/H} \Xi^{(b)}(\zeta) d\zeta. \end{aligned} \quad (\text{C.19})$$

As developed, we have three approximate forms of the velocity field  $\mathbf{u}$ , i.e.  $\mathbf{u} \approx \mathbf{U}^{(c)} \Xi^{(s)}$ ,  $\mathbf{u} \approx \mathbf{U}^{(c)} \Xi^{(b)}$  and  $\mathbf{u} \approx \mathbf{U}^{(c)} \Xi^{(q)}$ , and we must now compare these to the exact numerically determined form,  $\mathbf{u} = \mathbf{U}^{(c)} \Xi$ . Because the horizontal functions  $\mathbf{U}^{(c)}$  are the same across all test functions, it will be enough for us to assess the robustness of a given approximation by comparing the three vertical functions  $\Xi^{(s)}$ ,  $\Xi^{(b)}$  and  $\Xi^{(q)}$  against the numerically determined exact function  $\Xi$ . The left panel of Fig. C.16 shows the vertical structure functions discussed here and as compared to the exact solution determined using a Chebyshev integration method. We see that the exact solution  $\Xi$  is well approximated by  $\Xi^{(q)}$ . The right panel of the same figure also proves that  $\Xi^{(q)}$  is also well approximated by  $\Xi^{(b)}$ , the use of the latter which would incur errors of no more than 50%. The implication of this is that the flow rates and mass-fluxes are reasonably well approximated by a factor of 2 (i.e.,  $\sim \max(1/g_q)$ ) when utilizing the rates associated with the higher temperatures corresponding to the base of

<sup>10</sup> We realize that this is akin to mixing apples with oranges as  $\text{H}_2\text{O}$  ice has a different density and rheology compared to  $\text{N}_2/\text{CO}$  ice. If the amount of converted substrate bedrock is small compared to the volume of  $\text{N}_2/\text{CO}$  ice, then we consider the results here to be fair and representative of the effective volume present of transportable materials.

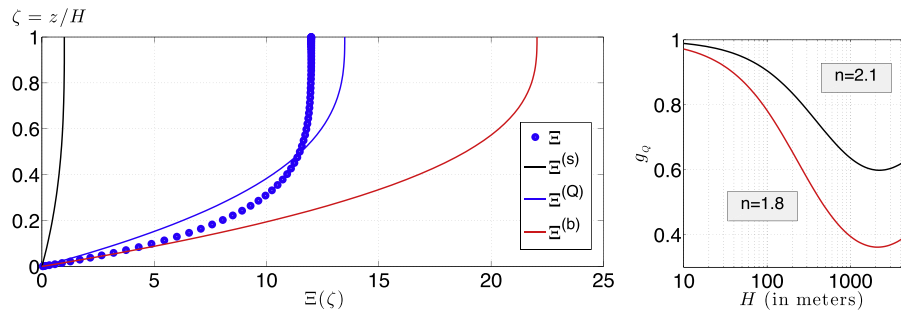


**Fig. C.16.** Left Panel: comparison of various approximate forms of  $\Xi$ . Figure shows the (scaled) vertical shear profile for a rheology with  $n = 1.8$ ,  $T_a = 1036$  K,  $\bar{T}_{0z} = 20$  K/km,  $T_s = 38.5$  K and a depth  $H = 250$  m. Exact solution (filled circles) compares best with  $\Xi^{(Q)}$ . Right Panel: The corrective factor  $g_0$  for the two rheologies considered in this paper. Red curve is appropriate for the  $N_2$  ice-grain rheology of Eluszkiewicz and Stevenson (1990) enhanced by dislocation accommodated GBS, where  $T_a = 1036$  K,  $n = 1.8$ , while the black curve is appropriate for the rheology of laboratory annealed  $N_2$  ice of Yamashita et al. (2010), where  $T_a = 426$  K,  $n = 2.1$ . (For interpretation of the references to color in this figure legend, the reader is referred to the web version of this article.)

the layer, i.e., by approximating the velocity field with end-state defined by the base of the layer,  $\mathbf{u} \approx \mathbf{U}^{(c)} \Xi^{(b)}$ .

Consequently, and from here on out, we adopt the approximate dry ice velocity field constructed from  $\Xi^{(Q)}$  and explicitly write out the analytical expressions for the dry components of the  $N_2$  ice mass-flux and velocities to be used in our numerical modeling hereafter: Beginning with the surface dry velocities we have,

$$\begin{aligned} \mathbf{U}(x, y, t) &\approx g_0 \exp\left[\frac{H/H_a}{1 + H/H_{\Delta T}}\right] \mathbf{U}^{(c)}(x, y, t) \\ &= g_0 \exp\left[\frac{H/H_a}{1 + H/H_{\Delta T}}\right] \frac{A_s H}{n+1} (\rho_s g H)^n \frac{S^{n-1} \nabla Z}{(1 + S^2)^{n/2}}, \end{aligned} \quad (\text{C.20})$$

whereupon, the vertically sheared total horizontal flow (dry plus sliding fields) becomes

$$\mathbf{u}(x, y, z, t) \approx \mathbf{u}_{sl} + \mathbf{U}(x, y, t) \Xi^{(c)}(z), \quad (\text{C.21})$$

where  $\Xi^{(c)}$  is as given in Eq. (C.13).

## References

- Anderson, R.S., Dühnforth, M., Colgan, W., Anderson, L., 2012. Far-flung moraines: exploring the feedback of glacial erosion on the evolution of glacier length. *Geomorphology* 179, 269–285. doi:10.1016/j.geomorph.2012.08.018.
- Ashby, M.F., Verrall, R.A., 1978. Micromechanisms of flow and fracture, and their relevance to the rheology of the upper mantle. *Philos. Trans. R. Soc. London Ser. A* 288, 59–93. doi:10.1098/rsta.1978.0006.
- Balmforth, N.J., Craster, R.V., Toniolo, C., 2003. Interfacial instability in non-Newtonian fluid layers. *Phys. Fluids* 15, 3370–3384. doi:10.1063/1.1611179.
- Benn, D.I., Evans, D.J.A., 2010. *Glaciers and Glaciation, 2nd Edition*. Routledge.
- Chandrasekhar, S., 1961. Oxford. Clarendon.
- Clayton, J.O., Giauque, W.F., 1932. The heat capacity and entropy of carbon monoxide: heat of vaporization. Vapor pressures of solid and liquid. *Free energy to 5000 K from spectroscopic data*. *J. Am. Chem. Soc.* 54, 2610–2626.
- Dobrovolskis, A.R., Harris, A.W., 1983. The obliquity of Pluto. *Icarus* 55, 231–235. doi:10.1016/0019-1035(83)90077-5.
- Dobrovolskis, A.R., Peale, S.J., Harris, A.W., 1997. *Dynamics of the Pluto-Charon binary*. Pluto Charon 159.
- Durham, W.B., Prieto-Ballesteros, O., Goldsby, D.L., Kargel, J.S., 2010. Rheological and thermal properties of icy materials. *Space Sci. Rev.* 153, 273–298. doi:10.1007/s11214-009-9619-1.
- Earle, A.M., Binzel, R.P., 2015. Pluto's insolation history: latitudinal variations and effects on atmospheric pressure. *Icarus* 250, 405–412. doi:10.1016/j.icarus.2014.12.028.
- Eluszkiewicz, J., 1991. On the microphysical state of the surface of Triton. *J. Geophys. Res.* 96, 19.
- Eluszkiewicz, J., Stevenson, D.J., 1990. Rheology of solid methane and nitrogen - applications of Triton. *Geophys. Res. Lett.* 17, 1753–1756. doi:10.1029/GL017i010p01753.
- Esteve, D., Sullivan, N.S., 1981. N.M.R. study of self-diffusion in solid  $N_2$ . *Solid State Commun.* 39, 969–971. doi:10.1016/0038-1098(81)90067-3.
- Fracassi, P.F., Cardini, G., O'shea, S., Impey, R.W., Klein, M.L., 1986. Solid and liquid carbon monoxide studied with the use of constant-pressure molecular dynamics. *Phys. Rev. B* 33, 3441–3447. doi:10.1103/PhysRevB.33.3441.
- Fray, N., Schmitt, B., 2009. Sublimation of ices of astrophysical interest: bibliographic review. *Planet. Space Sci.* 57, 2053–2080. doi:10.1016/j.pss.2009.09.011.
- Giauque, W.F., Clayton, J.O., 1933. The heat capacity and entropy of nitrogen: heat of vaporization. Vapor pressures of solid and liquid. *J. Am. Chem. Soc.* 55, 4875–4889.
- Gladstone, G.R., Stern, S.A., Ennico, K., Olkin, C.B., Weaver, H.A., Young, L.A., Summers, M.E., Strobel, D.F., Hinson, D.P., Kammer, J.A., Parker, A.H., Steffl, A.J., Linscott, I.R., Parker, J.W., Cheng, A.F., Slater, D.C., Versteeg, M.H., Greathouse, T.K., Retherford, K.D., Throop, H., Cunningham, N.J., Woods, W.W., Singer, K.N., Tsang, C.C.C., Schindhelm, E., Lisse, C.M., Wong, M.L., Yung, Y.L., Zhu, X., Curdt, W., Lavvas, P., Young, E.F., Tyler, G.L., Bagenal, F., Grundy, W.M., McKinnon, W.B., Moore, J.M., Spencer, J.R., Andert, T., Andrews, J., Banks, M., Bauer, B., Bauman, J., Barnouin, O.S., Bedini, P., Beisser, K., Beyer, R.A., Bhaskaran, S., Binzel, R.P., Birath, E., Bird, M., Bogan, D.J., Bowman, A., Bray, V.J., Brozovic, M., Bryan, C., Buckley, M.R., Buie, M.W., Buratti, B.J., Bushman, S.S., Calloway, A., Carcich, B., Conard, S., Conrad, C.A., Cook, J.C., Cruikshank, D.P., Custodio, O.S., Ore, C.M.D., Deboy, C., Dischner, Z.J.B., Dumont, P., Earle, A.M., Elliott, H.A., Ercol, J., Ernst, C.M., Finley, T., Flanigan, S.H., Fountain, G., Freeze, M.J., Green, J.L., Guo, Y., Hahn, M., Hamilton, D.P., Hamilton, S.A., Hanley, J., Harch, A., Hart, H.M., Hersman, C.B., Hill, A., Hill, M.E., Holdridge, M.E., Horanyi, M., Howard, A.D., Howett, C.J.A., Jackman, C., Jacobson, R.A., Jennings, D.E., Kang, H.K., Kaufmann, D.E., Kollmann, P., Krimigis, S.M., Kusnierkiewicz, D., Lauer, T.R., Lee, J.E., Lindstrom, K.L., Lunsford, A.W., Mallder, V.A., Martin, N., McComas, D.J., McNutt, R.L., Mehoke, D., Mehoke, T., Melin, E.D., Mutchler, M., Nelson, D., Nimmo, F., Nunez, J.I., Ocampo, A., Owen, W.M., Paetzold, M., Page, B., Pelletier, F., Peterson, J., Pinkine, N., Piquette, M., Porter, S.B., Protopapa, S., Redfern, J., Reitsema, H.J., Reuter, D.C., Roberts, J.H., Robbins, S.J., Rogers, G., Rose, D., Runyon, K., Ryschkewitsch, M.G., Schenk, P., Sepan, B., Showalter, M.R., Soluri, M., Stanbridge, D., Stryk, T., Szalay, J.R., Tapley, M., Taylor, A., Taylor, H., Umurhan, O.M., Verbiscer, A.J., Versteeg, M.H., Vincent, M., Webbert, R., Weidner, S., Weigle, G.E., White, O.L., Whittenburg, K., Williams, B.G., Williams, K., Williams, S., Zangari, A.M., Zirnstein, E., 2016. The atmosphere of Pluto as observed by New Horizons. *Science* 351, aad8866. doi:10.1126/science.aad8866.
- Glen, J.W., 1955. The creep of polycrystalline ice. *Proc. R. Soc. London Ser.A* 228, 519–538. doi:10.1098/rspa.1955.0066.
- Goluskin, D., Johnston, H., Flierl, G.R., Spiegel, E.A., 2014. Convectively driven shear and decreased heat flux. *J. Fluid Mech.* 759, 360–385. doi:10.1017/jfm.2014.577.1408.4802.
- Goodwin, R.D., 1985. Carbon monoxide thermophysical properties from 68 to 1000 K at pressures to 100 MPa. *J. Phys. Chem. Ref. Data* 14, 849–932. doi:10.1063/1.555742.
- Grundy, W.M., Binzel, R.P., Buratti, B.J., Cook, J.C., Cruikshank, D.P., Dalle Ore, C.M., Earle, A.M., Ennico, K., Howett, C.J.A., Lunsford, A.W., Olkin, C.B., Parker, A.H., Philippe, S., Protopapa, S., Quirico, E., Reuter, D.C., Schmitt, B., Singer, K.N., Verbiscer, A.J., Beyer, R.A., Buie, M.W., Cheng, A.F., Jennings, D.E., Linscott, I.R., Parker, J.W., Schenk, P.M., Spencer, J.R., Stansberry, J.A., Stern, S.A., Throop, H.B., Tsang, C.C.C., Weaver, H.A., Weigle, G.E., Young, L.A., 2016. Surface compositions across Pluto and Charon. *Science* 351, aad9189. doi:10.1126/science.aad9189.
- Hindmarsh, R.C.A., 2004. A numerical comparison of approximations to the Stokes equations used in ice sheet and glacier modeling. *J. Geophys. Res. (Earth Surf.)* 109, F01012. doi:10.1029/2003JF000065.
- Howard, A.D., 2007. Simulating the development of Martian highland landscapes through the interaction of impact cratering, fluvial erosion, and variable hydrologic forcing. *Geomorphology* 91, 332–363.
- Howard, A.D., Moore, J.M., Schenk, P.M., White, O.L., Spencer, J., 2012. Sublimation-driven erosion on Hyperion: topographic analysis and landform simulation model tests. *Icarus* 220, 268–276. doi:10.1016/j.icarus.2012.05.013.
- Hurle, D.T.J., Jakeman, E., Pike, E.R., 1967. On the solution of the Benard problem with boundaries of finite conductivity. *Proc. R. Soc. London Ser.A* 296, 469–475. doi:10.1098/rspa.1967.0039.
- Hughes, T., 2009. Thermal convection and the origin of ice streams. *J. Glaciol.* 55, 524–536. doi:10.3189/00214309788816722.
- Kelley, K., 1935. U.S. department of the interior bureau of mines. *Bulletin* 584.
- Kirk, R.L., 1990. Diffusion kinetics of solid methane and nitrogen: implications for Triton. In: *Lunar and Planetary Science Conference*, 21.

- Konstantinov, V.A., Manzhelii, V.G., Revyakin, V.P., Sagan, V.V., Pursky, O.I., 2006. Isochoric thermal conductivity of solid carbon oxide: the role of phonons and 'diffusive' modes. *J. Phys. Condens. Matter* 18, 9901–9909. doi:10.1088/0953-8984/18/43/011.
- Landuyt, W., Lerley, G., 2012. Linear stability analysis of the onset of sublithospheric convection. *Geophys. J. Int.* 189, 19–28. doi:10.1111/j.1365-246X.2011.05341.x.
- McKinnon, W.B., Nimmo, F., Wong, T., Schenk, P.M., White, O.L., Roberts, J.H., Moore, J.M., Spencer, J.R., Howard, A.D., Umurhan, O.M., Stern, S.A., Weaver, H.A., Olkin, C.B., Young, L.A., Smith, K.E., Moore, J.M., McKinnon, W.B., Spencer, J.R., Beyer, R., Buie, M., Buratti, B., Cheng, A., Cruikshank, D., Dalle Ore, C., Gladstone, R., Grundy, W., Howard, A., Lauer, T., Linscott, I., Nimmo, F., Olkin, C., Parker, J., Porter, S., Reitsema, H., Reuter, D., Roberts, J.H., Robbins, S., Schenk, P.M., Showalter, M., Singer, K., Strobel, D., Summers, M., Tyler, L., Weaver, H., White, O.L., Umurhan, O.M., Banks, M., Barnouin, O., Bray, V., Carcich, B., Chaikin, A., Chavez, C., Conrad, C., Hamilton, D., Howett, C., Hofgartner, J., Kammer, J., Lisse, C., Marcotte, A., Parker, A., Retherford, K., Saina, M., Runyon, K., Schindhelm, E., Stansberry, J., Steffl, A., Stryk, T., Throop, H., Tsang, C., Verbiscer, A., Winters, H., Zangari, A., G. a. I. T. T. New Horizons Geology, 2016. Convection in a volatile nitrogen-ice-rich layer drives Pluto's geological vigour. *Nature* 534, 82–85. doi:10.1038/nature18289.
- Moore, J.M., McKinnon, W.B., Spencer, J.R., Howard, A.D., Schenk, P.M., Beyer, R.A., Nimmo, F., Singer, K.N., Umurhan, O.M., White, O.L., Stern, S.A., Ennico, K., Olkin, C.B., Weaver, H.A., Young, L.A., Binzel, R.P., Buie, M.W., Buratti, B.J., Cheng, A.F., Cruikshank, D.P., Grundy, W.M., Linscott, I.R., Reitsema, H.J., Reuter, D.C., Showalter, M.R., Bray, V.J., Chavez, C.L., Howett, C.J.A., Lauer, T.R., Lisse, C.M., Parker, A.H., Porter, S.B., Robbins, S.J., Runyon, K., Stryk, T., Throop, H.B., Tsang, C.C.C., Verbiscer, A.J., Zangari, A.M., Chaikin, A.L., Wilhelm, D.E., Bagenal, F., Gladstone, G.R., Andert, T., Andrews, J., Banks, M., Bauer, B., Bauman, J., Barnouin, O.S., Bedini, P., Beisser, K., Bhaskaran, S., Birath, E., Bird, M., Bogan, D.J., Bowman, A., Brozovic, M., Bryan, C., Buckley, M.R., Bushman, S.S., Calloway, A., Carcich, B., Conrad, C.A., Cook, J.C., Custodio, O.S., Ore, C.M.D., Deboy, C., Dischner, Z.J.B., Dumont, P., Earle, A.M., Elliott, H.A., Ercol, J., Ernst, C.M., Finley, T., Flanigan, S.H., Fountain, G., Freeze, M.J., Greathouse, T., Green, J.L., Guo, Y., Hahn, M., Hamilton, D.P., Hamilton, S.A., Hanley, J., Harch, A., Hart, H.M., Hersman, C.B., Hill, A., Hill, M.E., Hinson, D.P., Holdridge, M.E., Horanyi, M., Howard, A.D., Howett, C.J.A., Jackman, C., Jacobson, R.A., Jennings, D.E., Kammer, J.A., Kang, H.K., Kaufmann, D.E., Kollmann, P., Krimigis, S.M., Kusnierkiewicz, D., Lauer, T.R., Lee, J.E., Lindstrom, K.L., Linscott, I.R., Lisse, C.M., Lunsford, A.W., Mallder, V.A., Martin, N., McComas, D.J., McNutt, R.L., Mehoke, D., Mehoke, T., Melin, E.D., Mutchler, M., Nelson, D., Nimmo, F., Nunez, J.I., Ocampo, A., Owen, W.M., Paetzold, M., Page, B., Parker, A.H., Parker, J.W., Pelletier, F., Peterson, J., Pinkine, N., Piquette, M., Porter, S.B., Protopapa, S., Redfern, J., Reitsema, H.J., Reuter, D.C., Roberts, J.H., Robbins, S.J., Rogers, G., Rose, D., Runyon, K., Retherford, K.D., Ryschkewitsch, M.G., Schenk, P., Schindhelm, E., Sepan, B., Showalter, M.R., Singer, K.N., Soluri, M., Stanbridge, D., Steffl, A.J., Strobel, D.F., Stryk, T., Summers, M.E., Szalay, J.R., Tapley, M., Taylor, A., Taylor, H., Throop, H.B., Tsang, C.C.C., Tyler, G.L., Umurhan, O.M., Verbiscer, A.J., Versteeg, M.H., Vincent, M., Webbert, R., Weidner, S., Weigle, G.E., White, O.L., Whittenburg, K., Williams, B.G., Williams, S., Woods, W.W., Zangari, A.M., Zirnstein, E., 2015. The Pluto system: initial results from its exploration by New Horizons. *Science* 350, aad1815. doi:10.1126/science.aad1815. 1510.07704.
- Trafton, L., 1984. Large seasonal variations in Triton's atmosphere. *Icarus* 58, 312–324. doi:10.1016/0019-1035(84)90048-4.
- Umurhan, O.M., Howard, A.D., Moore, J.M., Schenk, P.M., White, O.L., 2015. Reconstructing Helene's surface history – plastics and snow. In: *Lunar and Planetary Science Conference*. In: *Lunar and Planetary Science Conference*, 46, p. 2400.
- Umurhan, O.M., Moore, J.M., McKinnon, W.B., Howard, A.D., Nimmo, F., Grundy, W., Stern, S.A., Weaver, H., Olkin, C., Ennico, K., Young, L.A., 2015. Glacial flow on and onto Sputnik Planum. *DPS-47* 47. 210.11
- White, O.L., Schenk, P.M., Dombard, A.J., 2013. Impact basin relaxation on Rhea and Iapetus and relation to past heat flow. *Icarus* 223, 699–709. doi:10.1016/j.icarus.2013.01.013.
- Yamashita, Y., Kato, M., Arakawa, M., 2010. Experimental study on the rheological properties of polycrystalline solid nitrogen and methane: implications for tectonic processes on Triton. *Icarus* 207, 972–977. doi:10.1016/j.icarus.2009.11.032.
- Young, L.A., 2012. Volatile transport on inhomogeneous surfaces: I - analytic expressions, with application to Pluto's day. *Icarus* 221, 80–88. doi:10.1016/j.icarus.2012.06.032. 1205.1382.
- Robuchon, G., Nimmo, F., 2011. Thermal evolution of Pluto and implications for surface tectonics and a subsurface ocean. *Icarus* 216, 426–439. doi:10.1016/j.icarus.2011.08.015.